High-resolution hypernuclear spectroscopy at Jefferson Lab, Hall A

F. Garibaldi,[1,2] A. Acha,[3] P. Ambrozewicz,[3] K. A. Aniol,[4] P. Baturin,[5] H. Benaoum,[6] J. Benesch,[7] P. Y. Bertin,[8] K. I. Blomqvist,[9] W. U. Boeglin,[3] H. Breuer,[10] P. Brindza,[7] P. Bydžovský,[11] A. Camsonne,[8] C. C. Chang,[10] J.-P. Chen,[7] Seonho Choi,[12] E. A. Chudakov,[7] E. Cisbani,[1,2] S. Colilli,[1,2] L. Coman,[3] F. Cusanno,[1,*] B. J. Craver,[13] G. De Cataldo,[14] C. W. de Jager,[7,*] R. De Leo,[14] A. P. Deur,[13] C. Ferdi,[8] R. J. Feuerbach,[7] E. Folts,[7] S. Frullani,[1,*] O. Gayou,[15] F. Giuliani,[1,2] J. Gomez,[7] M. Gricia,[1,2] J. O. Hansen,[7] D. Hayes,[16] D. W. Higinbotham,[7] T. K. Holmstrom,[17] C. E. Hyde,[16,8] H. F. Ibrahim,[18] M. Iodice,[19] X. Jiang,[5] L. J. Kaufman,[20] K. Kino,[21] B. Kross,[7] L. Lagamba,[14] J. J. LeRose,[22] R. A. Lindgren,[13] M. Lucentini,[23] D. J. Margaziotis,[4] P. Markowitz,[3] S. Marrone,[14] D. G. Meekins,[7] Z. E. Meziani,[12] K. McCormick,[5] R. W. Michaels,[7] D. J. Millener,[24] T. Miyoshi,[25] B. Moffit,[17] P. A. Monaghan,[15] M. Moteabbed,[3] C. Muñoz Camacho,[26] S. Nanda,[7] E. Nappi,[14] V. V. Nelyubin,[13] B. E. Norum,[13] Y. Okasyasu,[25] K. D. Paschke,[20] C. F. Perdrisat,[17] E. Piasetzky,[27] V. A. Punjabi,[28] Y. Qiang,[15] B. Raue,[3] P. E. Reimer,[29] J. Reinhold,[3] B. Reitz,[7] R. E. Roche,[30] V. M. Rodriguez,[31] A. Saha,[7,*] F. Santavenere,[1,2] A. J. Sarty,[32] J. Segal,[7] A. Shahinyan,[33] J. Singh,[13] S. Širca,[34] R. Snyder,[13] P. H. Solvignon,[12,*] M. Sotona,[11,*] R. Subedi,[35] V. A. Sulkosky,[17] T. Suzuki,[25] H. Ueno,[36] P. E. Ulmer,[16] G. M. Urciuoli,[1] E. Voutier,[37] B. B. Wojtsekhowski,[7] X. Zheng,[29] and C. Zorn[7]
(Jefferson Lab Hall A Collaboration)

[1]*Istituto Nazionale di Fisica Nucleare, Sezione di Roma, Piazzale Aldo Moro 2, I-00185 Rome, Italy*
[2]*Istituto Superiore di Sanità, I-00161 Rome, Italy*
[3]*Florida International University, Miami, Florida 33199, USA*
[4]*California State University, Los Angeles, Los Angeles, California 90032, USA*
[5]*Rutgers, The State University of New Jersey, Piscataway, New Jersey 08855, USA*
[6]*Department of Applied Physics and Astronomy, University of Sharjah, United Arab Emirates*
[7]*Thomas Jefferson National Accelerator Facility, Newport News, Virginia 23606, USA*
[8]*Université Blaise Pascal/IN2P3, F-63177 Aubière, France*
[9]*Universität Mainz, Mainz, Germany*
[10]*University of Maryland, College Park, Maryland 20742, USA*
[11]*Nuclear Physics Institute, Řež near Prague, Czech Republic*
[12]*Temple University, Philadelphia, Pennsylvania 19122, USA*
[13]*University of Virginia, Charlottesville, Virginia 22904, USA*
[14]*Istituto Nazionale di Fisica Nucleare, Sezione di Bari and University of Bari, I-70126 Bari, Italy*
[15]*Massachussets Institute of Technology, Cambridge, Massachusetts 02139, USA*
[16]*Old Dominion University, Norfolk, Virginia 23508, USA*
[17]*College of William and Mary, Williamsburg, Virginia 23187, USA*
[18]*Cairo University, Giza 12613, Egypt*
[19]*Istituto Nazionale di Fisica Nucleare, Sezione di Roma Tre, I-00146 Rome, Italy*
[20]*University of Massachusetts Amherst, Amherst, Massachusetts 01003, USA*
[21]*Research Center for Nuclear Physics, Osaka University, Ibaraki, Osaka 567-0047, Japan*
[22]*Chesapeake Bay Governor's School, Tappahannock, Virginia 222560, USA*
[23]*Istituto Nazionale di Fisica Nucleare, Sezione di Roma, gruppo collegato Sanità, and Istituto Superiore di Sanità, I-00161 Rome, Italy*
[24]*Brookhaven National Laboratory, Upton, New York 11973, USA*
[25]*Tohoku University, Sendai, 980-8578, Japan*
[26]*CEA Saclay, DAPNIA/SPhN, F-91191 Gif-sur-Yvette, France*
[27]*School of Physics and Astronomy, Sackler Faculty of Exact Science, Tel Aviv University, Tel Aviv 69978, Israel*
[28]*Norfolk State University, Norfolk, Virginia 23504, USA*
[29]*Argonne National Laboratory, Argonne, Illinois 60439, USA*
[30]*Florida State University, Tallahassee, Florida 32306, USA*
[31]*University of Houston, Houston, Texas 77204, USA*
[32]*St. Mary's University, Halifax, Nova Scotia, Canada*
[33]*Yerevan Physics Institute, Yerevan, Armenia*
[34]*Faculty of Mathematics and Physics, University of Ljubljana, Slovenia*
[35]*Kent State University, Kent, Ohio 44242, USA*
[36]*Yamagata University, Yamagata 990-8560, Japan*
[37]*LPSC, Université Joseph Fourier, CNRS/IN2P3, INPG, F-38026 Grenoble, France*

(Received 6 July 2018; revised manuscript received 2 November 2018; published 10 May 2019)

[*]Deceased.

The experiment E94-107 in Hall A at Jefferson Lab started a systematic study of high-resolution hypernuclear spectroscopy in the $0p$-shell region of nuclei such as the hypernuclei produced in electroproduction on ^{9}Be, ^{12}C, and ^{16}O targets. In order to increase counting rates and provide unambiguous kaon identification, two superconducting septum magnets and a ring-imaging Cherenkov detector were added to the Hall A standard equipment. The high-quality beam, the good spectrometers, and the new experimental devices allowed us to obtain very good results. For the first time, measurable strength with sub-MeV energy resolution was observed for the core-excited states of $^{12}_{\Lambda}$B. A high-quality $^{16}_{\Lambda}$N hypernuclear spectrum was likewise obtained. A first measurement of the Λ binding energy for $^{16}_{\Lambda}$N, calibrated against the elementary reaction on hydrogen, was obtained with high precision, 13.76 ± 0.16 MeV. Similarly, the first $^{9}_{\Lambda}$Li hypernuclear spectrum shows general agreement with theory (distorted-wave impulse approximation with the SLA and BS3 electroproduction models and shell-model wave functions). Some disagreement exists with respect to the relative strength of the states making up the first multiplet. A Λ separation energy of 8.36 MeV was obtained, in agreement with previous results. It has been shown that the electroproduction of hypernuclei can provide information complementary to that obtained with hadronic probes and the γ-ray spectroscopy technique.

DOI: 10.1103/PhysRevC.99.054309

I. INTRODUCTION

The physics of hypernuclei, multibaryonic systems with nonzero strangeness, is an important branch of contemporary nuclear physics at low energy (structure, energy spectra, and weak decays of hypernuclei) as well as at intermediate energy (production mechanism) [1]. The Λ hypernucleus is a long-lived baryonic system (with a lifetime of $\approx 10^{-10}$ s) and provides us with a variety of nuclear phenomena. The hyperon inside an ordinary nucleus is not affected by the Pauli principle and can penetrate deeply inside the nucleus, permitting measurements of the system response to the stress imposed on it. The study of its propagation can reveal configurations, or states, not seen in other ways. The study also gives important insight into the structure of ordinary nuclear matter.

An understanding of baryon-baryon interactions is fundamental in order to understand our world and its evolution. However, our current knowledge is limited at the level of strangeness zero particles (p and n). Hence, studying the hyperon-nucleon (YN) and hyperon-hyperon (YY) interactions is very important in order to extend our knowledge and seek a unified description of them. Since very limited information can currently be obtained from elementary hyperon-nucleon scattering, hypernuclei are unique laboratories for studying the ΛN interaction [2]. In fact, an effective ΛN interaction can be determined from hypernuclear spectra obtained from various reactions and can be used to discriminate between different YN potentials employed to carry out *ab initio* many-body calculations [3].

Until now, a large body of data came from two types of highly complementary hypernuclear spectroscopy techniques: reaction-based spectroscopy with hadron probes and γ-ray spectroscopy [4]. Reaction spectroscopy, that directly populates hypernuclear states, reveals the level structure in the Λ bound region and can even study excited states between the nucleon emission threshold and the Λ emission threshold. It provides information on Λ hypernuclear structure and the Λ emission threshold. The information on Λ hypernuclear structure and the ΛN interaction is obtained through the determination of hypernuclear binding energies, excitation spectra, lifetimes, reaction cross sections, and their angular distributions. Moreover, precise measurements of the production cross sections provide information on the hypernuclear production mechanism and the dynamics of the elementary-production reaction. γ-ray spectroscopy achieves ultrahigh resolution (typically a few keV). It is a powerful tool for investigation of the spin-dependent part of the ΛN interaction that requires precise information on the level structure of hypernuclei. Both these powerful techniques have limitations, first limited energy resolution and small spin-flip amplitudes, and second the access only to hypernuclear states below the nucleon-emission threshold.

Experimental knowledge can be greatly improved using electroproduction of strangeness characterized by large three-momentum transfer ($\approx$250 MeV/c), large angular momentum transfer ΔJ, and strong spin-flip terms, even at zero production angles [4]. Moreover, the $K^{+}\Lambda$ pair production occurs on a proton in contrast to a neutron in (K^{-}, π^{-}) or (π^{+}, K^{+}) reactions, making possible the study of different hypernuclei and charge-dependent effects from a comparison of mirror hypernuclei (charge-symmetry breaking). The hypernuclear γ-ray measurements give extremely high-precision energy-level spacings, while the precision of the energy levels given by the $(e, e'K^{+})$ reaction spectroscopy can potentially be a few hundreds of keV, which is more than an order of magnitude worse. However, the advantage of being able to simultaneously observe more complete structures as well as to provide precise absolute binding energy is obvious. For transitions with energy larger than 1 MeV, Ge detector efficiency decreases quickly, and thus statistics becomes a major problem for the current γ-ray spectroscopy program using the Ge detector technique.

Even though plans for various new hypernuclear physics studies at other facilities exist, the precise and accurate mass spectroscopy from the JLab program has a unique position, in addition to the clearly known common advantages of electroproduction (such as the size of momentum transfer that allows large angular momentum transfer, extra spin transfer from the virtual photon, and converting a proton into a Λ to study neutron-rich hypernuclei).

The E94-107 experiment in Hall A at Jefferson Lab (see Ref. [5] for the proposal) started a systematic study of high-resolution hypernuclear spectroscopy on p-shell targets,

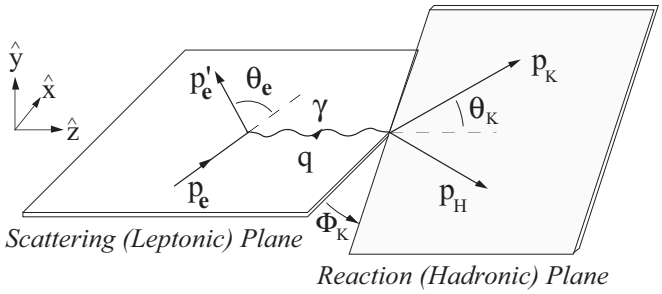

FIG. 1. Kinematics of hypernuclear electroproduction in the laboratory frame.

specifically ^{9}Be [6], ^{12}C [7], and ^{16}O [8]. Moreover, a study of the elementary reaction on a proton was performed.

This paper describes the experimental apparatus, the theoretical models, the results obtained, and the physics information extracted from them.

II. THE EXPERIMENT

Hall A at Jefferson Lab is well suited to perform $(e, e'K^+)$ experiments. Scattered electrons can be detected in the high-resolution spectrometer (HRS) electron arm while coincident kaons are detected in the HRS hadron arm [9]. The disadvantage of smaller electromagnetic cross sections with respect to hadron-induced reactions is partially compensated for by the high current, high duty cycle, and high energy-resolution capabilities of the beam. The detector packages for the electron and hadron spectrometers are almost identical, except for the particle identification (PID) systems discussed later [9].

The kinematics for the three experiments is shown in Fig. 1 and values are given in Table I. The beam and final electron energies are denoted E_i and E_f, respectively, $Q^2 = -q^2$ (q being the four-momentum defined in Fig. 1), and the electron (θ_e), kaon (θ_{Ke}), and photon ($\theta_{\gamma e}$) angles are measured with respect to the beam direction. The virtual photon energy, transverse polarization, and flux factor are denoted as E_γ, ϵ, and Γ. The kaon momentum p_K changes a little bit due to a different hypernucleus mass for the excited states. A coplanar experimental setup was chosen with the kaon azimuthal angle $\Phi_K = 180^\circ$. Then, the kaon laboratory angle with respect to the photon direction is $\theta_K = \theta_{Ke} - \theta_{\gamma e}$; see Fig. 1.

The reasons for this choice were the following. The momentum transfer to the hypernucleus in the electroproduction is rather large (350 MeV/c) and decreases steadily with increasing energy of the virtual photon ($E_\gamma = E_e - E_{e'}$) while the elementary electroproduction cross section, with the kaon detected at forward angles, is almost constant for $E_\gamma = 1.2$–2.2 GeV. The momentum transfer for forward kaon scattering angles falls from 330 MeV/c at $E_\gamma = 1.2$ GeV to 250 MeV/c at $E_\gamma = 2.5$ GeV, so that higher energies are preferable. Moreover, because the cross section depends strongly on Q^2 (through the virtual photon flux as determined by the electron kinematics), the measurements have to be made at low Q^2 to get reasonable counting rates. Hence, the electron scattering angle must be small, and the kaon angle must be close to the virtual photon direction in order to minimize the momentum transfer. Moreover, due to the long flight path in the HRS spectrometer, to keep a reasonable kaon survival fraction the kaon momenta must be fairly high.

Good energy resolution together with a low level of background is mandatory for this experiment. The energy resolution depends on the momentum resolution of the HRS spectrometers, on the straggling and energy loss in the target, and on the beam energy spread. A momentum resolution of the system (HRSs + septum magnets) of $\Delta p/p = 10^{-4}$ (FWHM) and a beam energy spread as small as 6×10^{-5} (FWHM) are necessary to be able to get an excitation energy resolution of 700 keV or better. A very good PID system is needed to guarantee a low level of background.

A. The beam

1. Beam monitors

E94-107 desired a continuous-wave, 3.66-GeV, 100-μA electron beam with very small energy spread and vertical spot size (energy spread $\sigma \leqslant 3 \times 10^{-5}$, spot size $\sigma \leqslant 100\ \mu$m). With some effort, the continuous electron beam accelerator facility (CEBAF) staff were able to achieve these requirements. The absolute value of the beam energy was measured using the arc method (see Sec. II A 2). The beamline is segmented into several sections isolated by vacuum valves. The beam diagnostic elements are those standard to all accelerators, including four-antenna position monitors, resonant cavities for current monitoring, wire scanners, insertable screens at 45° to the beam seen by external charge-coupled device (CCD) cameras, photomultiplier tubes (PMTs) external to the beam pipe used as beam-loss monitors, and two thin (250-nm) graphite foils at 45° to the beam, producing optical transmission radiation seen by external CCD cameras. The standard difference-over-sum technique is then used to determine the relative position of the beam to within 100 μm for currents above 1 μA [10,11]. The absolute position of the beam can be determined from the beam position monitors (BPMs) by calibrating them with respect to wire scanners (superharps) that are located adjacent to each of the BPMs (7.353 and 1.122 m upstream of the target). The wire scanners are surveyed with respect to the Hall A coordinates at regular intervals and the

TABLE I. Kinematics in the laboratory frame for the three experiments.

Target	E_i (GeV)	E_f (GeV)	θ_e (deg)	θ_{Ke} (deg)	E_γ (GeV)	$\theta_{\gamma e}$ (deg)	Q^2 (GeV^2)	ϵ	Γ [(GeV sr)$^{-1}$]	p_K (GeV)
^{9}Be	3.77	1.56	6	6	2.21	4.20	0.0644	0.703	0.0174	1.96
^{12}C	3.77	1.56	6	6	2.21	4.20	0.0644	0.703	0.0174	1.95–1.96
^{16}O	3.66	1.45	6	6	2.21	3.91	0.0581	0.682	0.0172	1.95–1.97

results are reproducible at the level of 200 μm. Drifts in the central beam energy were monitored using the so-called "Hall A Tiefenback energy" value (see Sec. II A 3). The beam spot size and the energy spread were continuously monitored using a synchrotron light interferometer (SLI) [12] (see Sec. II A 4).

2. The arc method

The arc method determines the energy by measuring the deflection of the beam in the arc section of the beamline. The nominal bend angle of the beam in the arc section is 34.3°. The measurement is made when the beam is tuned in dispersive mode in the arc section. The momentum of the beam is then related to the field integral of eight dipoles and the net bend angle through the arc section [9]. The method consists of two simultaneous measurements, one for the magnetic field integral of the bending elements and the other for the actual bend angle of the arc.

3. Hall A Tiefenback

The "Hall A Tiefenback" is a beam diagnostic tool developed by Mike Tiefenback of the JLab Accelerator Scientific staff [13]. Unlike the arc method above, the quadrupoles are left in their normal beam transport condition with peak dispersion of 4 m (over a 25-m length). There are no horizontal correctors in the arc, just the 3-m dipoles. The beam position monitor read backs, in concert with the dipole and quadrupole fields, are used to compute the beam energy at the center of the arc. No synchrotron radiation correction is needed at the low energies used in these experiments. Both methods rely on an accurate knowledge of the dipole fields. These were measured to 0.01% and there is a ninth dipole, in series with the eight in the arcs, with a nuclear magnetic resonance (NMR) sensor used to track changes due to hysteresis cycles in the decades since the measurement of the dipole magnetic fields.

4. Synchrotron light interferometer (SLI)

An SLI [14] has been used at Jefferson Lab in order to measure small beam sizes below the diffraction limit. The device is not invasive and can monitor the profile of the electron beam. The SLI at Jefferson Lab is a wave-front division interferometer that uses polarized quasi-monochromatic synchrotron light. The syncrotron light generated by the electron beam in the dipole magnet at the high dispersion point (4 m) of the Hall A bend is extracted through a quartz window. After this window, the light is optically shielded until it reaches a CCD video camera connected to the image processor. An optical system, comprising two adjustable 45° mirrors, a diffraction limited lens, and a movable double-slit assembly, produces an interferogram. The precision in energy-spread monitoring is $dE/E < 3 \times 10^{-5}$, as required by our experiment. The basic parameter to calculate the beam size is the visibility (V) of the interference pattern. The visibility is estimated from the intensities of the first (central) maximum ($I_{\max}$) and minima ($I_{\min}$) of the interferogram,

$$V = \frac{I_{\max} - I_{\min}}{I_{\max} + I_{\min}}. \quad (1)$$

Assuming a Gaussian beam shape, the energy spread of the beam can be calculated.

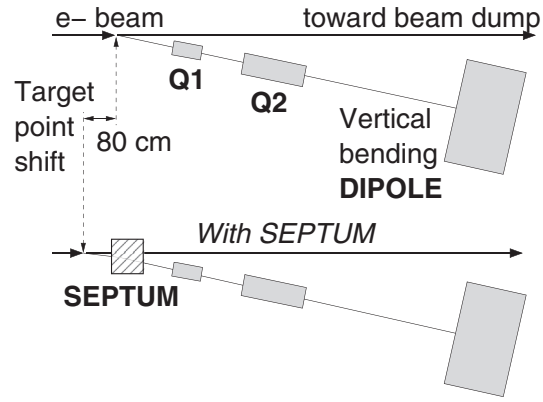

FIG. 2. Schematic layout of the modifications to the HRS setup.

5. Rastered beam

To avoid melting the beryllium target and the beryllium windows delimiting the waterfall target, beams with a rectangular raster pattern and a uniform raster density distribution were used on these targets. This raster system allowed the use of beam currents as high as 100 μA by distributing the heat load caused by the beam impact on the targets.

B. Spectrometers and septum magnets

The standard-equipment HRS pair [9] in Hall A was designed to deliver the required momentum resolution. However, because the hypernuclear cross section falls rapidly with increasing angle (momentum transfer), the minimum angles with respect to the beamline of 12.5° were too large. Physically, the first quadrupole (Q1) of the HRSs cannot be moved closer than 12.5° to the beam without hitting the beam pipe. This shortcoming was mitigated by the introduction of a pair of superconducting septum magnets, providing a 6.5° horizontal bend each. By moving the target position 80 cm upstream and inserting the septum magnets on either side of the beamline, the target seems to be situated on the optical axis of the two spectrometers (see Fig. 2). This is precisely true only for the central momentum of the spectrometer. For other momenta, the target will appear to be shifted sideways. The septa were designed in such a way that the trajectory of the particle in Fig. 2 scattered at acceptance central angle ϕ would overlap, after being bent, the line originating from O (old target position) and making an angle θ ($\geqslant$12.5°) with the beam line. In addition, that septum gap has to be designed to accept all particles scattered in the acceptance cone (see Fig. 3 for the case $\theta = 6°$, $\phi = 12.5°$, and an acceptance in the midplane of 24 mrad).

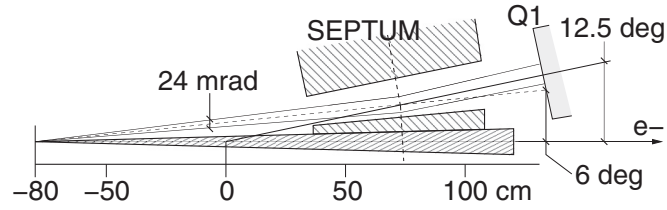

FIG. 3. Layout of the septum insertion.

Thus, the HRS pair at 12.5° on either side of the beamline is able to detect kaons and electrons at 6° (see Fig. 2). This new spectrometer configuration (septum + HRS) provides a general-purpose device that extends the HRS features to small scattering angles while preserving the spectrometer optical performance [15].

The septum magnets have to fulfill the following requirements. They must match the entrance optics of the HRS spectrometers for a pivot displaced by 0.8 m upstream of the target in an angular range of 6° to 12.5°. The septa must bend particles of momentum up to 4 GeV/c of either polarity at any angle from 6° to 12.5° and match the HRS optics from 12° to 24°. The unique location of the septa at the match point, the short space between the displaced scattering chamber and the first HRS quadrupole, and the proximity to the outgoing electron beam impose severe space constraints. The septum field quality is determined by an experimental resolution requirement of overall $\Delta p/p = 10^{-4}$. Optical simulations allowed us to verify that the magnetic system is consistent with preservation of spectrometer performance. For details of the design and construction of the septum magnets, see Ref. [15].

A very nice feature of the septum magnet setup was that the two arms were essentially independent and could be tuned and optimized separately. Because of their small bend angle and relatively short length (80 cm), the septum magnets made only a modest perturbation on the standard HRS optics that was easily corrected by a small tuning of the three quadrupoles in each arm.

The HRSs with the septum magnets allow determination of the secondary electrons and produced kaon parameters through

$$\mathbf{Y} = T \cdot \mathbf{X}, \tag{2}$$

whose explicit form is

$$Y_i = \sum_{klmn} T_i^{klmn} (X_1)^k (X_2)^l (X_3)^m (X_4)^n, \tag{3}$$

where $i =$ 1,2,3,4; k, l, m, and n are non-negative integers; and the T_i^{klmn} are real numbers.

In the equation above, T is a tensor, usually called the optical database; $\mathbf{Y}$ is the array composed of δ_0, the percentage difference between the particle momentum and the momentum of the spectrometer central trajectory, Y_0, the position along the target of the particle scattering point, and θ_0 and ϕ_0, the angles that identify the particle direction just after its scattering off the target

$$\mathbf{Y} = \begin{pmatrix} \delta_0 \\ Y_0 \\ \theta_0 \\ \phi_0 \end{pmatrix}; \tag{4}$$

and $\mathbf{X}$ is the array made up of the particle coordinates x_f and y_f at the spectrometer focal plane and θ_f and ϕ_f that are the angles that define the particle trajectory when it hits the focal plane

$$\mathbf{X} = \begin{pmatrix} x_f \\ y_f \\ \theta_f \\ \phi_f \end{pmatrix}. \tag{5}$$

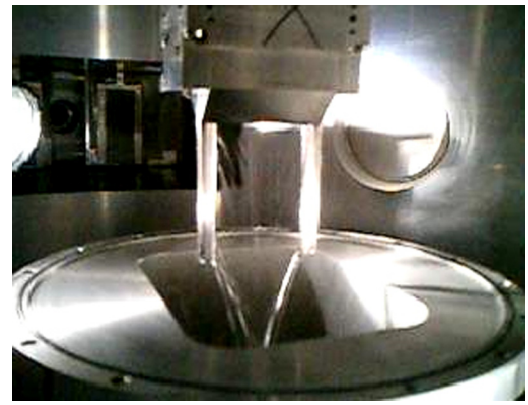

FIG. 4. View of the target cell with the waterfall.

C. Targets

A standard cryogenic target [9] was used for the study of the elementary reaction. Standard solid targets (100 mg/cm^2) were used for ^{9}Be and ^{12}C. A waterfall target system was used for experiments on ^{16}O [16]. This target has also been used for studying the elementary reaction.

The waterfall target system provides a target for experiments on ^{16}O. Using a waterfall for oxygen experiments has many advantages. Pure oxygen is difficult to handle, as it is highly reactive. The use of other oxygen compounds requires additional measurements to subtract the nonoxygen background, whereas the hydrogen in water can be used for calibration purposes. The technique of using continuously flowing water as an electron-scattering target was first developed by Voegler and Friedrich [17] and later refined by Garibaldi *et al.* [16]. The waterfall foil is produced in a cell mounted in the standard scattering chamber. Water forced through slits forms a flat rectangular film that is stable as a result of surface tension and adherence to stainless steel poles (see Fig. 4). The water, continuously pumped from a reservoir, goes through a heat exchanger into the target zone and then back into the reservoir. All parts in contact with the water are made of stainless steel. Once the target is formed, the thickness increases with the pump speed up to a maximum value that depends on the dimension of the slits and the stainless steel poles [16]. A factor of ≈3 magnification is possible (see Fig. 5).

The target thickness stability is monitored by continuously measuring the pump speed, the flow rate, and the scattered electron rate. The target is designed to stay at a fixed angular position. Care has to be taken in choosing the window material because of the risk of melting for high beam currents (50 μA in this case). The entrance and exit windows are circular (30 mm in diameter) and made of Be (75 μm thick). Because Be is highly toxic, it has been plated with 13 μm of Ni and a monolayer of Au (that also serves to improve heat conductivity). Under the cell, a target frame holds up to five solid targets. A target position can be selected remotely by a mechanical system driven by stepping motors and controlled by absolute encoders whose precision is 0.1 mm.

The presence of the hydrogen has many advantages. In particular, it permits a calibration of the missing-mass scale

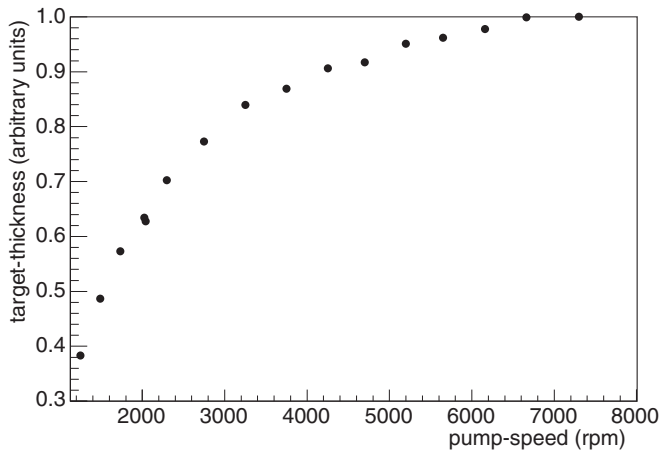

FIG. 5. Target thickness vs pump speed.

and thus an accurate measurement of the Λ-binding energy in the hypernucleus. The Λ-peak position from the reaction on hydrogen can be obtained using the nominal central values for the kinematic variables and then constrained to be zero, the expected position, by applying a small shift to the energy of the beam (the quantity with the largest uncertainty). This shift is common to reactions on hydrogen and oxygen and therefore its uncertainty does not affect the determination of the binding energies of the ${}^{16}_{\Lambda}$N levels.

D. Detector package

The detector packages of the two spectrometers are designed to perform various functions that include triggering to activate the data-acquisition electronics, collecting tracking information (position and direction), precise timing for time-of-flight measurements and coincidence determination, and identification of the scattered particles. The timing information as well as the main trigger is provided from scintillators. The particle identification is obtained from threshold Cherenkov-type detectors (aerogel and gas) and lead-glass shower counters. The main part of the detector package in the two spectrometers (trigger scintillators and vertical drift chambers) is identical. For details, see Ref. [9].

1. Tracking

Tracking information is provided by a pair of vertical drift chambers (VDC) in each HRS, described in detail in Ref. [18]. The concept of VDCs fits well into the HRSs, which are spectrometers with small acceptances, allowing a simple analysis algorithm and high efficiency because multiple tracks are rare. The position of each VDC relative to the box beam can be reproduced to within 100 μm. Each VDC chamber is composed of two wire planes separated by about 335 mm; in a standard UV sense-wire configuration, the wires of each successive plane are oriented at 90° to one another, and lie in the laboratory horizontal plane. They are inclined at an angle of 45° with respect to the dispersive and nondispersive directions. The nominal particle trajectory crosses the wire planes at an angle of 45°. The average thickness of all material encountered by particles in one chamber is 7.8×10^{-4} radiation lengths (X_0). The dominant single contribution to multiple scattering is the horizontal Ti window at the exit of the spectrometer vacuum, with a thickness of 127 μm ($5 \times 10^{-3}\, X_0$) [19]. In the focal plane, the position resolution is $\sigma_{x/y} \sim 100$ μm and the angular resolution is $\sigma_{\theta/\phi} \sim 0.5$ mrad. During the experiment, the VDCs ran very stably.

2. Triggering

There are two primary trigger scintillator planes (S1 and S2), separated by a distance of about 2 m. The time resolution per plane is approximately 0.50 ns (σ). For experiments that need a high hadron trigger efficiency, an additional scintillator trigger counter (S0) can be installed. The information from the gas Cherenkov counter can be added into the trigger. A coincidence trigger is made from the time overlap of the two spectrometer triggers in a logical AND unit. The various trigger signals go to the trigger supervisor module, which starts the data-acquisition readout.

3. Particle identification (PID)

a. Time of flight (TOF). The long path from the target to the HRS focal plane (25 m) allows accurate time-of-flight identification in coincidence experiments if the accidental rate is low. After correcting for differences in trajectory lengths, a TOF resolution of ≈0.5 ns (σ) is obtained. The time of flight between the S1 and S2 planes is also used to measure the speed of particles, β, with a resolution of 7% (σ).

b. Shower counters. Two layers of shower detectors [9] are installed in each HRS. The blocks in both layers in HRS-L and in the first layer in HRS-R are oriented perpendicular to the particle tracks. In the second layer of HRS-R, the blocks are parallel to the tracks. Typical pion rejection ratios of 500:1 are achieved using two-dimensional cuts of the energy deposited in the front layer versus the total energy deposited.

c. Gas Cherenkov. A gas Cherenkov detector filled with CO_2 at atmospheric pressure [20] is mounted between the trigger scintillator planes S1 and S2. The detector allows an electron identification with 99% efficiency and has a threshold for pions at 4.8 GeV/c. The detector has ten lightweight spherical mirrors [21] with 80 cm focal length, each viewed by a photomultiplier tube (PMT) (Burle 8854). The focusing of the Cherenkov ring onto a small area of the PMT photocathode leads to a high current density near the anode. To prevent a nonlinear PMT response even in the case of few photoelectrons requires a progressive high-voltage divider. The length of the particle path in the gas radiator is 130 cm for the gas Cherenkov in the HRS-R, leading to an average of about twelve photoelectrons. In the HRS-L, the gas Cherenkov detector in its standard configuration has a path length of 80 cm, yielding seven photoelectrons on average. The total amount of material in the particle path is about 1.4% of the radiation length (X_0). Because of its reduced thickness, the resolution in HRS-L is not as good as that of the shower detector in HRS-R. The combination of the gas Cherenkov and shower detectors provides a pion suppression above 2 GeV/c of a factor of 2×10^{-5}, with a 98% efficiency for electron selection in the HRS-R.

d. Aerogel Cherenkov. There are two aerogel Cherenkov counters available with different indices of refraction that can be installed in either spectrometer and allow a clean separation of pions, kaons, and protons over the full momentum range of the HRS spectrometers. The aerogel is continuously flushed with dry CO_2 gas. The two counters (A1 and A2) are diffusion-type aerogel counters. A1 has 24 PMTs (Burle 8854). The 6-cm-thick aerogel radiator used in A1 has a refractive index of 1.015, giving a threshold of 2.84 (0.803) GeV/c for kaons (pions). The average number of photoelectrons for GeV electrons in A1 is ≈8. The 9-cm-thick aerogel radiator used in A2 has a refractive index of 1.055, giving a threshold of 1.55 (2.94) GeV/c for kaons (protons). It is viewed by 26 PMTs (Burle 8854). Trigger logic is used to require that A1 does not fire (e.g., rejecting pions) but that A2 does fire (requiring kaons). Rejection factors of 70:1 for rejecting pions and >60:1 for protons were achieved using the aerogel counters in the hardware trigger.

e. Ring imaging Cherenkov detector (RICH). In order to reduce the background level in the produced spectra, a very efficient PID system is necessary for achieving an unambiguous kaon identification. In the electron arm, the gas Cherenkov counters provide pion rejection ratios up to 10^3. The dominant background (knock-on electrons) is reduced by a further two orders of magnitude by the lead glass shower counters, giving a total pion rejection ratio of 10^5. The standard PID system in the hadron arm is composed of two aerogel threshold Cherenkov counters [9,22] ($n_1 = 1.015$, $n_2 = 1.055$). Charged pions (protons) with momenta around 2 GeV/c are above (below) the Cherenkov light emission threshold. Kaons emit Cherenkov light only in the detector with the higher index of refraction. Hence, a combination of the signals from the two counters should distinguish among the three species of hadrons. However, because of inefficiencies and δ-ray production, the identification of kaons could be significantly contaminated by pions and protons, resulting in an unacceptable signal-to-noise ratio in the physics spectra. For these reasons, the need for an unambiguous identification of kaons has driven the design, construction, and installation of a RICH detector in the hadron HRS focal plane detector package. The layout of the RICH is conceptually identical to a large ion collider experiment (ALICE) high-momentum PID (HMPID) design [23]. A detailed description of the layout and the performance of the RICH detector can be found in Refs. [24–26]. It uses a proximity-focusing geometry (no mirrors involved), a CsI photocathode, and a 15-mm-thick liquid perfluorohexane radiator [23]. Figure 6 shows the layout and the working principle of the adopted solution. The Cherenkov photons, emitted along a conic surface in the radiator, are refracted by the perfluoro-hexane (C_6F_{14})-quartz-methane interface and strike a cathode plane segmented in small pads after traversing a proximity gap of 10 cm filled with pure methane. The photon detector is made of a multiwire proportional chamber (MWPC), with one cathode formed by the pad planes allowing for the two-dimensional localization of the photon hit. Three photocathode modules of dimensions 640 × 400 mm^2 segmented in 8 × 8.4 mm^2 pads are assembled together for a total length of 1940 mm. The pad planes are covered by a thin (300 nm) substrate of CsI that acts as

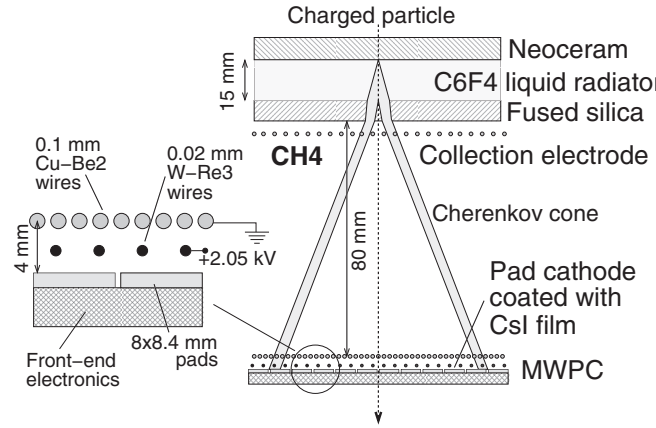

FIG. 6. Layout and working principle of the freon CsI proximity focusing RICH.

photon converter. The emitted photoelectron is accelerated by an electrostatic field between the pad plane (the cathode of the MWPC) and an anode wire plane at a distance of 2 mm from it. The induced charge on the pads is read out by a front-end electronics based on GASSIPLEX chips. A total number of 11520 pad channels are read out by CAEN VME V550 Flash ADC modules [23].

The RICH worked successfully during the experiment [27] where hadrons were detected in the momentum range $p = 1.96 \pm 0.1$ GeV/c. The average number of photoelectrons detected for pions is $N_\pi = 13$ while for protons $N_p = 8$, their ratio being in perfect agreement with the expected ratio of produced photons at 1.96 GeV/c. In Fig. 7, the reconstructed Cherenkov angle distributions are reported. In the top panel, the angular distributions have been obtained using samples of π^+, K^+, and p as selected by the two aerogel counters. The kaon selected sample is practically not visible due to the very high pion-to-kaon ratio. For the dominant contribution of pions, the obtained angle resolution is $\sigma_c = 5$ mrad, in

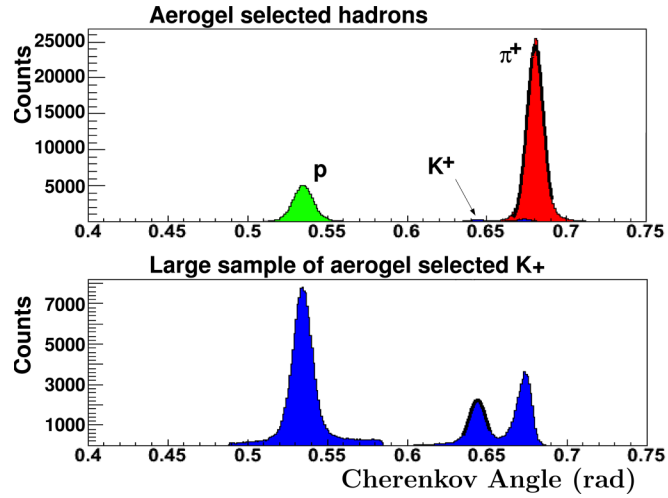

FIG. 7. Cherenkov angle distributions for protons (0.54 rad), kaons (0.64 rad), and pions (0.68 rad). The particle identification technique is explained in the text.

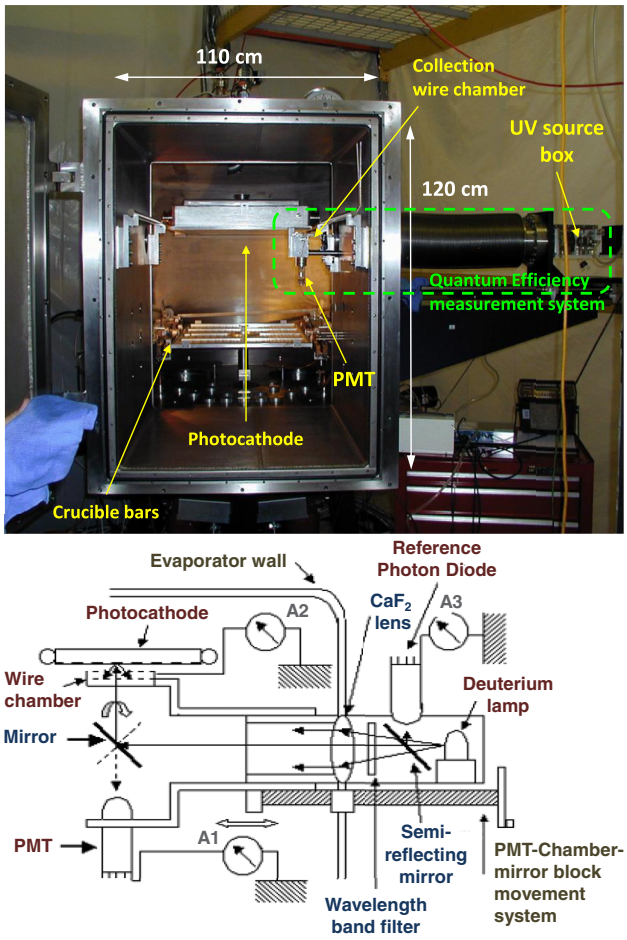

FIG. 8. The CsI evaporator system.

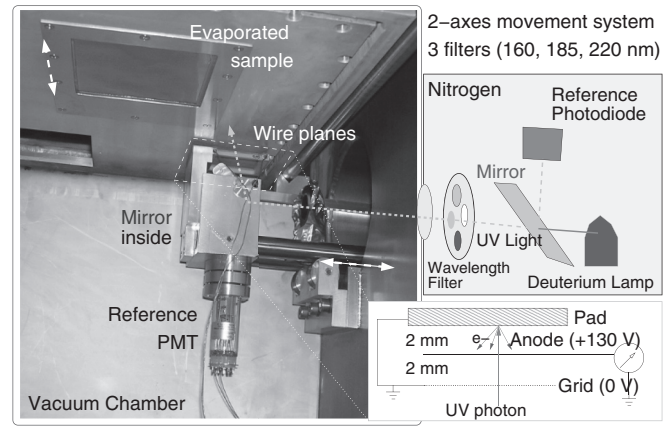

FIG. 9. The quantum-efficiency measurement system. The quantum efficiency ($\mathcal{Q}$) is given by $\mathcal{Q} = (I_{\text{chamber}}/I_{\text{PMT}})\,\mathcal{Q}_{\text{PMT}}$, where the ratio of measured currents in the wire chamber and PMT multiplies the quantum efficiency of the calibrated reference PMT (see text).

agreement with Monte Carlo simulations [27]. The kaon contribution is shown in the bottom panel where a large sample of aerogel kaon selected events has been used. The reconstructed Cherenkov angle variable can be clearly used to get rid of the pion and proton contamination. With a resolution $\sigma_c = 5$ mrad, the separation between pions and kaons is about 6σ. The performance reported here has been obtained with a measured quantum efficiency of about 25% at 160 nm [26]. The RICH pion rejection factor can be estimated to be ≈1000 from the pion peak content reduction factor.

f. The evaporator. A dedicated facility has been built for CsI evaporation of large-area photocathodes for the RICH detector. It consists of a cylindrical stainless steel vessel (110 cm high, 120 cm in diameter) equipped with four crucibles containing CsI powder (see Fig. 8). A vacuum of a few 10^{-7} mbar can be reached in less than 24 h. The prepolished pad plane (a printed circuit with three layers of metals, nickel, copper, and gold, glued on the vetronite substrate) is housed in the vacuum chamber and heated to 60° C usually for 12–24 h. The location of the crucibles with respect to the photocathode and their relative distance are optimized to ensure a minimum variation in thickness of 10% using equal amount of CsI in each crucible. The CsI powder evaporates at a temperature of ≈500 °C. In order to monitor the quality of the evaporation and its uniformity, an online quantum-efficiency measuring system has been built and successfully employed [26] (see Fig. 9). A movement system allows us to map out the entire photocathode. A deuterium lamp has been used as an UV source light. The UV collimated beam (1 cm in diameter) is split by means of a semitransparent mirror in such a way as to allow monitoring of the lamp emission by measuring the current from a photodiode. Three narrow-band filters (25 nm FWHM spread) selecting 160, 185, and 220 nm have been employed. The UV beam is sent, through a rotatable mirror, to the photocathode. The photocurrent, generated by electrons extracted from the CsI film, is detected with a small (5×5 cm^2) wire chamber located at a distance of 2 mm from the photocathode. The wires have a collection voltage of 133 V. A second wire plane, behind the first and oriented perpendicular to it, is kept at ground potential to obtain good charge collection on the first plane. After measuring the wire-chamber photocurrent (A2), the light is sent to a calibrated PMT, used in diode mode (A1), by rotating the mirror. The currents (1250-nA range) are measured by a picoammeter (KEITHLEY 485). The ratio of the currents $A2/A1$, multiplied by the PMT quantum efficiency, gives the "absolute" quantum efficiency of the photocathode. Following the prescription of the ALICE HMPID evaporation system, we have operated our system in such a way as to deposit a 300-nm CsI film. This thickness should guarantee safe operation of photocathode. In fact, no difference in quantum efficiency has been observed in the 150- to 700-nm range [26]. The thickness of 300 nm

has been chosen as a compromise for having a "stable" photocathode, while avoiding charging up problems at high radiation fluxes. An evaporation speed of 2 nm/s has been chosen as a compromise between the need to avoid CsI dissociation (high crucible temperature, high speed) and the need to avoid residual gas pollution on the CsI film surface [26].

III. DATA ANALYSIS

A. Binding energy reconstruction

Event by event, the values of the binding energy were reconstructed by using the detected momenta in the HRS arms and the incident beam energy. The binding energy is computed from

$$E_H = E_e - E_{e'} + M_A - E_K, \tag{6}$$

$$\mathbf{p}_H = \mathbf{p}_e - \mathbf{p}_{e'} - \mathbf{p}_K, \tag{7}$$

$$E_{\text{bind}} = M_{A-1} + M_\Lambda - \sqrt{E_H^2 - \mathbf{p}_H^2}. \tag{8}$$

Here, M_A is the target mass, M_{A-1} is the mass of the core nucleus (target minus a proton), and the momenta (and the corresponding energies) are defined as in Fig. 1 for the incoming and outgoing particles. B_Λ is defined as E_{bind} when the hypernucleus is in its ground state.

The central value and the spread of the beam energy were continuously monitored by OTR (optical transition radiation) or SLI measurements and by the Hall A Tiefenback measurement, respectively. Those values were added to the data stream every 30 s.

B. Event selection

In the selection of the events, significant data reduction is obtained by applying track quality selections and the PID requisites on the threshold Cherenkov counters, shower counters, and RICH detector. Only events in which the particle traveling HRS-L was a kaon and the particle traveling HRS-R was an electron were selected.

In addition, selection on the value of the HRS-L/HRS-R coincidence time (2-ns window) were applied to the event in order to be included in the calculation of the missing-energy spectrum. Events corresponding to invalid values of OTR or SLI were excluded.

C. Particle identification (PID)

As pointed out previously, the PID capability of the HRSs, basically guaranteed by TOF, by shower counters in HRS-R, and by aerogel counters in the HRS-L, is not sufficient for unambigous kaon identification. A RICH was built for this purpose. The fundamental role of the RICH in identifying the kaons is shown in Fig. 10.

In the left panel, the unfilled timing spectrum of coincidences between the electron and the hadron spectrometers, obtained by selecting for kaons using the two threshold aerogel counters, shows a barely visible kaon signal with a dominant contribution from misidentified pions and protons. The flat part of this spectrum is given by random coincidences. The 2-ns structure is a reflection of the pulse structure of the electron beam. The filled spectrum and its exploded version (right panel) is obtained by adding the RICH to the kaon selection. Here, all contributions from pions and protons completely vanish.

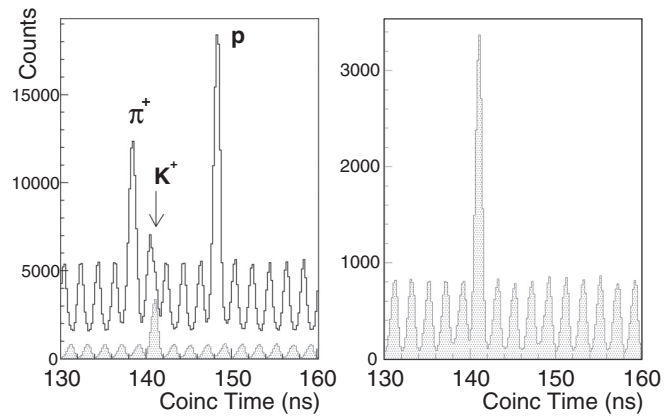

FIG. 10. Hadron plus electron arm coincidence time spectra. Left panel: The unfilled histogram is obtained by selecting kaons with only the threshold aerogel Cherenkov detectors. The filled histogram (expanded in the right panel) also includes the RICH kaon selection. The remaining contamination is due to accidental $(e, e') \otimes (e, K^+)$ coincidences. The π and p contamination is clearly reduced to a negligible contribution.

The crucial role of the RICH can be seen also from Fig. 11 that clearly shows that the excited states of $^{12}_{\Lambda}$B based on the 2.125-MeV $(1/2^-)$ and 5.020-MeV $(3/2^-)$ states of the ^{11}B

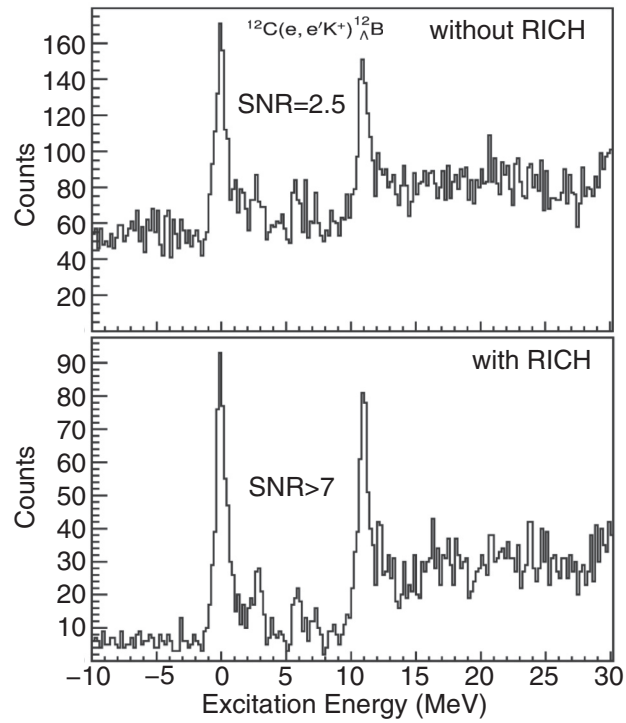

FIG. 11. Excitation energy spectra of $^{12}_{\Lambda}$B using, for kaon identification, only the aerogel (upper plot) or also the RICH (lower plot). The counts are for 200-keV bins.

core (see Fig. 18) are only barely seen if the RICH is not used in the analysis. In that case, the signal-to-noise ratio is insufficient.

D. RICH

A new particle rejection algorithm based on the χ^2 test was employed with the RICH used in the E94-107 experiment to distinguish kaons from pions and protons. It can be essentially summarized in the following steps (more details can be found in Ref. [28]).

(1) *Identification of the minimum ionizing particle (MIP) and Cherenkov photon hit points on the RICH cathode.* When a MIP crosses the RICH and the Cherenkov photons generated in the RICH radiator hit the RICH cathode plane, the pads near their hit points on the cathode generate charge signals. In the following, we refer to the single series of contiguous cathode pads fired by the MIP and the Cherenkov photons on the RICH cathode plane as clusters. The cluster corresponding to the MIP hit point is easily identified by calculating the interception point between the particle track provided by the drift chambers located on the focal plane of the HRS spectrometer and the RICH pad plane. The maximum charge cluster inside a defined radius R around this point was assumed to be the one generated by the MIP. The other clusters on the cathode could be generated either by a Cherenkov photon hitting the pad plane or by noise. For a particle of defined type (proton, kaon, or pion) crossing the RICH, Cherenkov photons could hit the cathode plane only in a determinate region. The distance between the center of this region and the MIP on the cathode plane depends only on the known particle momentum. The region boundaries depend on the experimental uncertainties of particle momentum, Cherenkov emission point in the RICH radiator, and other experimental uncertainties. For each particle crossing the RICH, there were hence only three regions, each corresponding to one of the three particle hypotheses, where Cherenkov photons could hit the cathode plane. Only clusters included in these three regions were considered as candidates to be generated by Cherenkov photons.

(2) *Cluster resolving.* The presence of two or more relative maxima in the geometric distribution in the RICH cathode plane of the pad signals of one single cluster indicated that that cluster was produced by two or more Cherenkov photons whose hit points on the cathode plane were so close that their corresponding clusters geometrically overlapped. These clusters were resolved (that is, decomposed into their constituent clusters) by assuming that they were generated by a number of Cherenkov photons equal to the number of pad-collected charge relative maxima in the cluster. The charge assigned to each of the single clusters constituting an unresolved cluster was proportional to the charge of the corresponding relative maximum.

(3) *Single-photon Cerenkov angle determination.* Using an algorithm based on a geometrical back-tracking, the emission angle of each single Cherenkov photon generated by the MIP in the RICH radiator was determined via two parameters: first, the relative position, in the RICH cathode pad plane, of the Cherenkov photon cluster and the MIP cluster, and second, the direction of the particle track with respect to the normal to the RICH cathode pad plane.

(4) *Particle identification based on the χ^2 test.* After the MIP cluster identification and the determination of N Cherenkov angles by the back-tracking from the N resolved cluster candidates had been performed, three χ^2 tests were performed, one for each of the three possible hypotheses (proton, kaon, or pion) for the MIP crossing the RICH. It was assumed that the measured Cherenkov angle distribution around its true value can be approximated with good accuracy by a Gaussian distribution. As a consequence, the sum $\chi^2 = \sum_i (\theta_{\text{expected}} - \theta_i)^2/\sigma^2$, with θ_i being the ith Cherenkov angle measurement, σ being the Cherenkov angle measurement standard deviation, and θ_{expected} being the expected Cherenkov photon emission angle according to the particle hypothesis, is expected to follow the χ^2 distribution if the particle hypothesis is correct and no cluster generated by electronic noise was present. The particle was hence identified with the one whose corresponding θ_{expected} value was such that the related χ^2 test provided a result acceptable within a predefined confidence level. If none of the three χ^2 tests was acceptable, this meant that electronic noise was present and one, two, ..., M terms in the χ^2, starting with the largest contributor to the χ^2, were iteratively removed until (at least) one of the three χ^2 values, and hence of the particle hypotheses, was compatible with the significance level.

(5) *Particle identification based on the single-photon Cherenkov angle average calculation.* Complementary to the particle identification based on the χ^2 test was the traditional identification based on the calculation of the average of the N θ_i measurements. This average, when the electronic noise is negligible, is distributed around the true value with a standard deviation equal to $\sigma/\sqrt{N}$ and hence its comparison with the three expected Cherenkov emission angles corresponding to the three-particle hypotheses is a powerful particle identification method.

(6) *Particle identification based on the combined use of the χ^2 test and of the single-photon Cerenkov angle average calculation.* The χ^2 test is a test on the variance of the N Cherenkov angle measurement's Gaussian distribution. The check on the average of the N Cherenkov angle measurements is a test on the mean of this distribution. The mean and variance of a Gaussian distribution are independent parameters. It can be mathematically demonstrated that the χ^2 test and the test on the average of the N Cherenkov angle measurements are hence two independent tests and can be used simultaneously to obtain proton and

pion rejection factors nearly equal to the product of the single test rejection factors, with the deviation from an exact product being due to analysis speed considerations and the presence of electronic noise.

(7) *Use of the aerogel Cerenkov detectors for an independent complete PID.* The Cherenkov detectors were used in addition to the RICH to obtain a proton and pion contamination smaller than 10^{-5} [28] with a negligible kaon detection inefficiency.

The combined use of the two algorithms provided, in combination with the thresholds of the two aerogel Cerenkov detectors, a completely satisfactory pion rejection ratio greater than 30 000 with practically no loss of statistics.

Based on checks against expected values of the average and the variance of the experimental measurements (two statistically independent variables), this algorithm can be employed not only with the RICH but whenever one deals with detectors that provide independent multiple measurements of variables with a constant probability distribution function.

E. Normalization

In order to calculate absolute cross sections, the missing energy spectrum has to be properly normalized. The cross section for a level i is computed as

$$\sigma_i = \frac{N_i}{l\ \mathrm{surv}(k)\epsilon_e\epsilon_k\epsilon_{\mathrm{coinc}}\Delta_e\Delta_k\Delta p_e}, \tag{9}$$

where N_i is the number of counts in the level i, corrected for the dead time, l is the luminosity, surv(k) is the kaon survival probability inside the left arm of HRS, ϵ_e and ϵ_k are the detector efficiencies for the two HRS arms, $\epsilon_{\mathrm{coinc}}$ is the efficiency of the coincidence trigger, Δ_e and Δ_k are the HRS geometric acceptances for the two arms, and Δp_e is the momentum acceptance for electrons.

Since we consider bound states, p_k and p_e are correlated and the cross section is integrated on the full range of Δp_k.

The luminosity is controlled by means of beam-current monitors and rates of single tracks in HRS arms. The dead time is controlled by means of proper data acquisition software. Detector efficiencies are controlled by specific analysis software.

F. Beam current

The measurement of beam current is crucial for cross section determination. For this purpose, the beamline is equipped with two beam-current monitors about 24.5 m upstream of the target (see Sec. II A 1). A beam-current monitor is a cylindrical resonant cavity made of stainless steel with a resonant frequency matching the frequency of the electron beam. We used the average value of the two beam-current monitors for our luminosity calculations.

G. Singles rates

Rates of tracks in single HRS arms were continuously monitored in order to cross-check the stability of the luminosity and the proper operation of the detectors. If a run period was showing anomalous values of single rates, it was excluded from the cross-section calculation.

H. Efficiency

We calculated the efficiency of the counter detectors based on the Poisson distribution. Then, the efficiency for an array of photoelectron detectors is $\epsilon = 1 - e^{-N_{p.e.}}$, where $N_{p.e.}$ is the number of detectors.

The efficiency of the RICH detector was determined by the use of clean track selection on A1 and A2. For the other components of the detector package, the standard procedures established for the HRS were used [9].

The stability of the detector efficiency was continuously monitored for each component of the HRS package. In fact, the track rates of the individual detectors were compared to the corresponding luminosity.

I. Peak search

A χ^2-based method was used for the detection of the peaks in the missing-energy spectra. This method analyzes energy bins in the spectrum and the width of the bins is variable in a range consistent with the energy resolution of the experiment. The background in the region of interest is very well reproduced by a linear fit. Then, for each energy bin showing an excess of counts with respect to the background, the confidence level of those counts was compared to the fluctuation of the corresponding background. If the confidence level was larger than 99% and a local maximum was found, then the corresponding energy region was fitted with a Gaussian or Voigt curve.

J. Energy resolution

Since the energy resolution is critical for the experimental results, the best computation of all the terms involved in the calculation of the missing energy has to be as precise as possible. Therefore, the following are needed:

(1) The optical database (see Sec. II B) for both the HRS arms has to provide the best momentum resolution in an acceptance range as large as possible.
(2) The beam-energy spread was continuously monitored using OTR and SLI in order to exclude the events when the energy spread was not good.
(3) The central beam energy was continuously monitored.
(4) In the case of a rastered beam (see Sec. II A 5), a software procedure was used to evaluate the real position of the incident electrons, to correspondingly compute the entrance position of the particles in the HRS and thus their momentum.
(5) An iterative method to check the presence of an unphysical dependence of the missing mass on the scattering variables was performed.

K. Radiative corrections

Standard radiative unfolding procedures were performed for ${}^{12}_{\Lambda}$B [7] and ${}^{16}_{\Lambda}$N [8] hypernuclei while, because of the more complicated structure of the spectrum, a different and

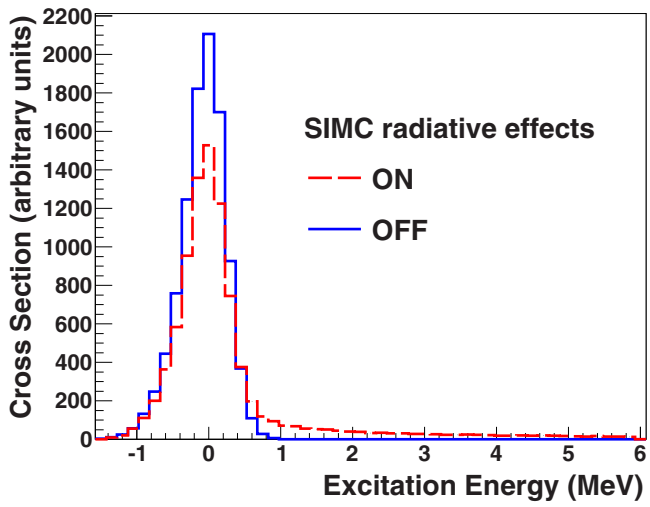

FIG. 12. From Ref. [6]. One peak of the excitation energy spectrum of the hypernucleus ${}^{9}_{\Lambda}$Li obtained through the reaction ^{9}Be$(e, e'K^{+})^{9}_{\Lambda}$Li as predicted by the Monte Carlo SIMC when including all effects (dashed red curve) and turning off the radiative effects (solid blue curve). The position of the peak has been made coincident with the ground state.

relatively new technique was used for ${}^{9}_{\Lambda}$Li. Here we summarize briefly this technique. Details can be found in Ref. [6]. In the case of ${}^{9}_{\Lambda}$Li, we have utilized the property, mathematically demonstrated in Appendix A of Ref. [6], that the subtraction of radiative effects from an experimental spectrum does not depend on the hypothesis or choice of the peak structure used to fit the spectrum itself, providing that the fit is good enough. This property is very useful when the peak structure underlying an experimental spectrum is uncertain, several theoretical (or simply hypothetical) peak structures fit the experimental spectrum well, and it is not obvious which of these structures is the right one. The ^{9}Be$(e, e'K^{+})^{9}_{\Lambda}$Li reaction with the E94-107 experimental apparatus was simulated with the Monte Carlo code called SIMC [29]. A single excitation-energy peak produced by this simulation is shown by the red curve in Fig. 12 (position and amplitude of the peak are arbitrary). The same figure shows, as a blue curve, a single excitation-energy peak produced by Monte Carlo SIMC simulations in the same conditions but with radiative effects "turned off." Several peak configurations, with different number, position, and heights of peaks like the one reproduced by the red curve of Fig. 12, fit the ${}^{9}_{\Lambda}$Li experimental energy spectrum. Because of the properties of the subtraction of radiative effects from spectra quoted above, all of them produced the same radiative-corrected spectrum determined by turning off the radiative corrections in the SIMC simulations, that is, by substituting the Fig. 12 red curve-like peaks with peaks like the one reproduced by the blue curve of Fig. 12. Because the Monte Carlo fits to the experimental spectrum were not perfect, slightly different radiative corrected spectra were obtained from the different peak configurations. The biggest of these differences was assumed as the systematic error generated in the reconstruction of the radiative corrected spectrum by the method employed to generate it. This systematic error was in any case negligible compared to the statistical error.

The unfolding of radiative corrections has been done bin by bin. Defining the "radiative corrected Monte Carlo" (RCMC) spectrum as the radiative-corrected spectrum obtained with the procedure described above and the "regular Monte Carlo" (RMC) spectrum as the spectrum produced by the SIMC simulations without turning off radiative corrections that fits the experimental spectrum (this spectrum could be obtained, as quoted above, with different peak configurations), the content of each bin of the radiative-corrected spectrum was obtained by multiplying the corresponding bin of the experimental spectrum by the correction factor given by the ratio of the RCMC spectrum and the RMC spectrum for that bin. In order to avoid possible removals of background enhancements or to artificially zero the spectrum in the regions where the RCMC spectrum was zero, the ratio between the RCMC spectrum and the RMC spectrum was performed after summing the background for each of them. The background value was then subtracted from the result of the product of the ratio with the corresponding bin.

Once the radiative corrections were applied, the binding-energy peak FWHM is small enough to clearly show the three-peak structure, shown in Fig. 17.

L. Calibrations

1. Optics

The quality and exact character of the optical transformation tensor were measured with a series of elastic scattering measurements using a 2-GeV electron beam on C and Ta targets. Measurements were also made using a sievelike mask in front of each spectrometer to optimize and calibrate the angular reconstruction. Finally, a check on residual correlations between the missing energy and the optical variables was performed by a dedicated iterative method. This method [30] was based on the property that any change in the optical database corresponds mathematically to an addition to the missing-mass numeric value of a polynomial in the scattering coordinates of the secondary electron and of the produced kaon. The method consisted of checking whether the numerical missing-mass value produced by the optical database had unphysical mathematical dependencies on the electron and kaon scattering variables. We fit these mathematical dependencies with a polynomial P, and the method consisted of finding the change in the optical database that produced an addition to the calculated numerical value of the missing mass equal to $-P$ and that hence eliminated the unphysical missing-mass dependency. Once any possible dependency of the numerical value of the missing mass on the scattering coordinates had been eliminated with the method described above, the optical database was optimized. Any further change in the optical database would have meant the addition of a polynomial in the scattering coordinates to the numerical value of the missing mass that would have produced new unphysical dependencies. The method described above is based on physics considerations. It also usually produces the best resolution. Unphysical dependencies of the missing-mass numerical value on the scattering coordinates means that

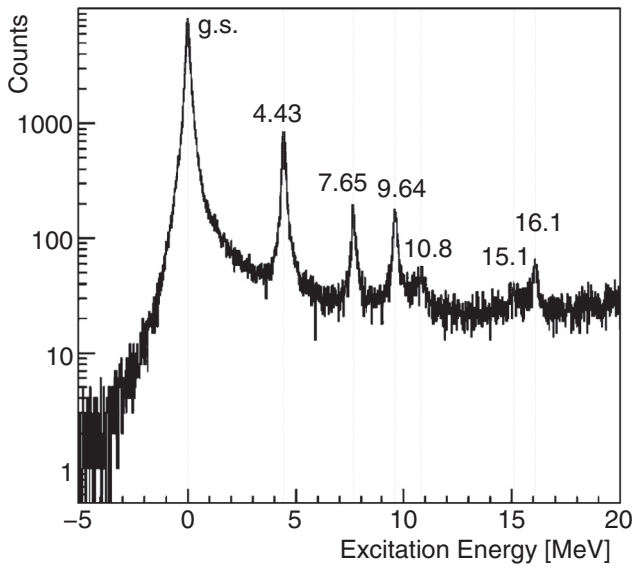

FIG. 13. Elastic ^{12}C scattering spectrum as seen in one arm of the HRS + septum configuration after optimization. The width of all the peaks, elastic and inelastic, is 10^{-4} (FWHM).

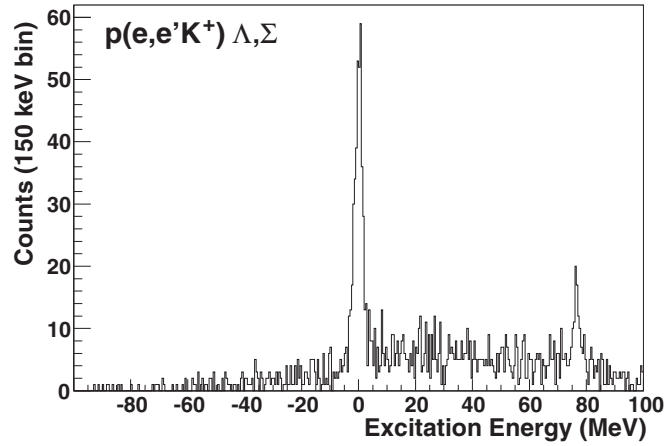

FIG. 14. Excitation energy spectrum of the $p(e, e'K^+)\Lambda$, Σ^0 on hydrogen used for energy-scale calibration. The fitted positions (not shown on the plot) for the peaks are -0.04 ± 0.08 MeV and 76.33 ± 0.24 MeV.

the missing-mass values as produced by the optical database spread around the true binding-energy values as a function of the scattering coordinates increasing the FWHM of the missing-energy spectrum peaks.

The method is conceptually similar to the one used to minimize the uncertainties on the kinematic variables described in Appendix B of Ref. [6]. The results of the calibration and optimization effort are illustrated in Fig. 13.

2. Waterfall target

A calibration of the target thickness as a function of pump speed has been performed. The thickness was determined from the elastic cross section on hydrogen [16]. The target thickness used was 75 ± 3 (stat.) ± 12 (syst.) mg/cm^2.

3. Energy scale

Careful calibration methods were employed to determine the binding-energy spectra of the hypernuclei $^{16}_{\Lambda}$N and $^{9}_{\Lambda}$Li, and of the excitation-energy spectrum of the hypernucleus $^{12}_{\Lambda}$B. These methods were necessary because the actual kinematics of the processes producing the hypernuclei quoted above differed from the nominal ones by amounts that would have produced significant shifts and distortions in binding-energy and excitation-energy spectra if proper measures had not been taken. The actual kinematics values in the experiment, provided by the CEBAF accelerator electron beam energy and by the central momenta and angles of the HRS electron and hadron arms, were essentially constant for the entire course of the experiments. The variances were of the order of 10^{-5} for the CEBAF electron-beam energy and the central momenta of the HRS electron and hadron arms, and practically zero for the spectrometer central angles. The values differed by unknown amounts from their nominal values, that is, the values to which the CEBAF beam energy and the HRS central momenta and angles were nominally set. Although small (the experimental uncertainties on the CEBAF accelerator electron-beam energy and on the spectrometer central momenta were of the order of 10^{-4} to 10^{-3} and those on the spectrometer central angles of the order of 10^{-2}), these kinematical uncertainties have two non-negligible effects: (a) they cause global shifts in the binding-energy spectra and (b) they cause peak distortions increasing the FWHM in the binding- and excitation-energy spectra. The actual kinematics values are then those that position states at their known value in binding- and excitation-energy spectra and minimize peak FWHMs.

To calibrate the binding-energy scale for $^{16}_{\Lambda}$N, the Λ peak position from the reaction on hydrogen was first obtained using the nominal central values for the kinematic variables and then constrained to be zero by applying a small shift to the energy of the beam (the quantity with the largest uncertainty). This shift is common to reactions on hydrogen and oxygen and therefore its uncertainty does not affect the determination of the binding energies of the $^{16}_{\Lambda}$N levels. A resolution of 800-keV FWHM for the Λ peak on hydrogen was obtained. The linearity of the scale has been verified from the $\Sigma^0 - \Lambda$ mass difference of 76.9 MeV. For this purpose, a few hours of calibration data were taken with a slightly lower kaon momentum (at fixed angles) to have the Λ and Σ^0 peaks within the detector acceptance. Figure 14 shows the two peaks associated with $p(e, e'K^+)\Lambda$ and $p(e, e'K^+)\Sigma^0$ production. The linearity is verified to $(76.9–76.4 \pm 0.3)/76.4 = 0.65 \pm 0.40\%$.

The hypernuclei $^{12}_{\Lambda}$B and $^{9}_{\Lambda}$Li were produced in one run where waterfall or hydrogen targets were not available. For these two hypernuclei, the energy-scale calibration was performed by positioning, in the $^{12}_{\Lambda}$B binding-energy spectrum, the ground-state peak at its known value of -11.37 MeV determined by emulsion data, after taking into account the additional shift in the energy scale (calculated through Monte Carlo simulations), caused by the energy losses in the target ^{12}C of the particles in the reaction producing the hypernucleus $^{12}_{\Lambda}$B. The kinematical uncertainties were further reduced by

minimizing the width of the $^{12}_{\Lambda}$B ground-state peak. This peak is actually a doublet with its two components separated by ≈160 keV (from the separation in $^{12}_{\Lambda}$C of 161.5 keV [31] and assuming charge symmetry). However, this value is small enough with respect to the energy resolution of the experiment to make the approximation of taking the $^{12}_{\Lambda}$B ground state as a single peak still valid and make consequently small the distortions incidental to the minimization of the FWHM of a peak that is actually a doublet. No attempt to minimize the FWHM was performed on the other peaks of the $^{12}_{\Lambda}$B spectrum. Because the hypernuclei $^{12}_{\Lambda}$B and $^{9}_{\Lambda}$Li were produced with the same apparatus and the same nominal kinematic variables, the $^{12}_{\Lambda}$B excitation-energy calibration results were applied to obtain the $^{9}_{\Lambda}$Li binding-energy spectrum, after accounting for the different particle-energy losses in the ^{12}C and ^{9}Be targets (calculated using the SIMC [29] package).

M. Systematic errors

The main sources of systematic errors in the missing-energy spectrum are the following:

(1) the uncertainty in the value of the beam energy,
(2) the uncertainty in the values of the track momenta, and
(3) the uncertainty in correction for radiative effects.

If not specified, our systematic errors on the position of the peaks in the missing-energy spectrum are negligible with respect to their corresponding statistical errors.

For the calculation of the binding energies, an additional contribution to the systematic error has to be considered, because of the need for an absolute energy scale. In the case of $^{12}_{\Lambda}$B, the binding energies were not calculated. In the case of $^{16}_{\Lambda}$N, this contribution is determined by the uncertainty in the position of the Λ peak obtained from the strangeness production on hydrogen in the waterfall target. In the case of $^{9}_{\Lambda}$Li, an additional contribution to the systematic error is due to the uncertainty of the knowledge of the $^{12}_{\Lambda}$B ground-state binding energy that we used as a reference.

For the calculation of absolute cross sections, the following sources of systematic uncertainties were considered:

(1) The uncertainty in the integrated beam current.
(2) The uncertainty in the target thickness. It is 2% for solid targets. For the oxygen in the waterfall target it is 16% as previously quoted.
(3) The uncertainty in the detector efficiencies.
(4) The uncertainty in the dead-time correction.
(5) The uncertainty in the HRS phase space.
(6) The uncertainty in the corrections for radiative effects.

Based on the run-by-run fluctuations, we evaluated our global systematic error on absolute cross sections as being within 15% for $^{12}_{\Lambda}$B and within 20% for $^{16}_{\Lambda}$N and $^{9}_{\Lambda}$Li. Because of the different contributions of the radiative effects, systematic errors were individually calculated for each peak in the missing-energy spectra.

IV. THEORY

A. Electroproduction of hypernuclei in DWIA

Production of hypernuclei by a virtual photon associated with a kaon in the final state can be satisfactorily described in the distorted-wave impulse approximation [32] because the photon and kaon momenta are rather high (≈1 GeV). The cross section for the production of the ground or excited states of a hypernucleus depends on the many-particle matrix element between the nonrelativistic wave functions of the target nucleus (Ψ_A) and the final hypernucleus (Ψ_H)

$$T^{\mu}_{if} = \langle \Psi_H | \sum_{j=1}^{Z} \chi_\gamma \chi^*_K J^{\mu}_j | \Psi_A \rangle. \tag{10}$$

Here J^{μ}_j is the hadronic current corresponding to electroproduction of a Λ on the proton (the elementary production). The sum runs over the protons of the target nucleus as we study K^+ electroproduction. In the one-photon approximation, the virtual photon is described by the function χ_γ proportional to the product of the wave functions of incoming and outgoing electrons without Coulomb distortion. The kaon distorted wave χ_K is calculated in the eikonal approximation from a first-order optical potential in which the density of the hypernucleus is approximated by that of the target nucleus. The eikonal approximation is sufficient for weakly interacting kaons with momenta larger than 1 GeV.

The kaon-nucleus optical potential is constructed using the kaon-nucleon total cross section and the ratio of the real to imaginary parts of the forward-scattering KN amplitude. The amplitude is properly isospin averaged to take into account the number of protons and neutrons in the nucleus. The KN amplitudes for isospin 0 and 1 are calculated in a separable model [33] with partial waves $l = 0, 1, \ldots, 7$ and with parameters recently fitted to the phase shifts and inelasticity parameters in the KN scattering. The nuclear density in the potential is modeled by the harmonic-oscillator form with the constant taken from experiments on nuclear charge radii.

The matrix element is calculated in the frozen-nucleon approximation (the target proton three-momentum in the laboratory frame is zero) that significantly simplifies the integration and allows one to express the elementary amplitude in the laboratory frame via only six Chew-Goldberger-Low-Nambu (CGLN) amplitudes [32]. To go beyond this factorization approach, i.e., include also a Fermi motion in the nucleus, one would have to calculate the elementary amplitude in a general reference frame that would, together with the momentum integration, make the calculation considerably more complicated.

Experiments on electroproduction of hypernuclei are performed in the kinematical region of almost real photons ($Q^2 = -q^2_\gamma \approx 0$). In this kinematics, the elementary electroproduction cross section is dominated by its transverse part and can be approximated by the photoproduction cross section, e.g., as in Ref. [34]. However, even at values of Q^2 as small as those in Table I, the transverse-longitudinal interference contribution can be important. That is why in the calculations presented here the full electroproduction cross section is used [32].

B. Elementary production process

The hadronic current, expressed in the nonrelativistic two-component formalism via six CGLN amplitudes in the laboratory frame, is calculated using an isobar model [32,35]. Because of the strong damping of the hypernuclear production cross section by the nucleus-hypernucleus form factors for large kaon angles, the dominant contribution from the elementary amplitudes comes from the region of very small kaon angles. In this kinematical region, however, the various isobar models give large differences in predicted cross sections, especially for $E_\gamma^{\rm lab} > 1.7$ GeV [34,36,37]; see also Sec. V A. The magnitude of these differences constitutes an important part of the theoretical uncertainty in predicting the hypernuclear production rate. For the energies of the Hall A experiments, $E_\gamma^{\rm lab} = 2.2$ GeV, the Saclay-Lyon model [38] gives very good results for the hypernuclear cross sections [6–8]. In our analysis, we also use a very recent isobar model BS3 [39] that fits the new data on photo- and electroproduction well (see Ref. [39] for more details on the data set) and also gives reasonable predictions for the cross sections at small kaon angles. Note that the recent JLab data on the Q^2 dependence of the separated transverse and longitudinal cross sections [40] are significantly better described by the BS3 model than by the Saclay-Lyon (SLA) model as is shown in Fig. 13 of Ref. [39]. However, it should be said that the data of Ref. [40] appeared long after the SLA model was made.

C. Nucleus and hypernucleus wave functions

The wave functions for light hypernuclei are obtained from shell-model calculations using an effective p-shell interaction to describe the nuclear core states [41]. In this weak-coupling approach, both Λ and Σ hyperons in s states are coupled to p-shell core wave functions optimized to fit a wide range of p-shell properties. The ΛN effective interaction can be written in the form

$$V_{\Lambda N}(r) = V_0(r) + V_\sigma(r)\mathbf{s}_\Lambda \cdot \mathbf{s}_N + V_\Lambda(r)\mathbf{l}_{\Lambda N} \cdot \mathbf{s}_\Lambda + V_N(r)\mathbf{l}_{\Lambda N} \cdot \mathbf{s}_N + V_T(r)\, S_{12}, \quad (11)$$

where V_0 is the spin-averaged central interaction, V_σ is the spin-dependent central term, V_Λ and V_N are the spin-orbit interactions, and V_T is the tensor ΛN interaction with $S_{12} = 3(\boldsymbol{\sigma}_\Lambda \cdot \mathbf{r}/r)(\boldsymbol{\sigma}_N \cdot \mathbf{r}/r) - \boldsymbol{\sigma}_\Lambda \cdot \boldsymbol{\sigma}_N$. A quadratic spin-orbit term, also allowed by symmetries, is neglected.

For a p-shell nucleon and a hyperon (Λ or Σ) in the s orbit, the radial integrals can be parameterized via five constants, $\bar{V}$, Δ, S_Λ, S_N, and T, that have a one-to-one correspondence with the five $p_N s_\Lambda$ two-body matrix elements. By convention, S_Λ and S_N are actually the coefficients of $\mathbf{l}_N \cdot \mathbf{s}_\Lambda$ and $\mathbf{l}_N \cdot \mathbf{s}_N$ (see the discussion of Eqs. (2.8) and (2.9) in Ref. [42]). The last four matrix elements can be determined from the analysis [41,43,44] of precise γ-ray spectra of p-shell hypernuclei obtained via hypernuclear γ-ray spectroscopy, mostly with the Hyperball [4]. The ΣN and ΛN-ΣN coupling matrix elements can be parametrized in the same way with the values of the parameters calculated using Woods-Saxon wave functions and Gaussian or Yukawa representations of YN G-matrix elements based on free YN baryon-baryon potentials [43]. The Λ-Σ coupling makes significant contributions to hypernuclear doublet spacings but, while included in the shell-model calculations, is not important for analyses of $(e, e'K^+)$ data.

Unfortunately, γ-ray spectroscopy is feasible only for hypernuclear states lying below particle thresholds. Information about the structure of multiplets above particle-emission thresholds, generally when the Λ is in a p orbit, is provided by analyses of the missing-mass spectra from electroproduction (reaction spectroscopy) that can be realized with better energy resolution than from the $\pi^\pm$ or K^- induced production reactions [4].

After the partial-wave decomposition of the wave functions $\chi_\gamma \chi_K^*$, the many-body matrix element (10) can be expressed by means of the hypernucleus-nucleus structure constants, radial integrals, and the CGLN amplitudes. The structure constants are calculated from one-body density matrix elements provided by the shell-model structure calculations with the interaction (11). In the radial integrals, we make use of Woods-Saxon single-particle wave functions for the target proton and final Λ that we suppose to be a more realistic approximation than the harmonic oscillator wave functions, especially in the case of weakly bound particles. The parameters, the radius, slope, and potential depth of the Woods-Saxon potential, that include the central, spin-orbit, and Coulomb parts, are taken from other processes. The single-particle binding energies correspond to the particle separation energies.

The two-body matrix elements for hyperons in $0p$ orbits (20 matrix elements for $p_N p_\Lambda$) for use in the shell-model calculations (with Λ-Σ coupling included) are likewise calculated using Woods-Saxon wave functions.

D. Isobar and Regge-plus-resonance models

The elementary electroproduction process can be described by isobar models based on an effective Lagrangian with only hadronic degrees of freedom [35,38,39,45–47]. Another approach, suited also for description above the resonance region up to $E_\gamma^{\rm lab} \approx 16$ GeV, is the Regge-plus-resonance model [48] (RPR) that combines the Regge model [49], appropriate to description above the resonance region ($E_\gamma^{\rm lab} > 4$ GeV), with elements of the isobar model eligible for the low-energy region. Both approaches are one-channel descriptions that neglect interactions in the final state and thus violate unitarity. However, they are suitable for more complex calculations of electroproduction of hypernuclei [34].

Generally, the production amplitude can be split into a resonant and nonresonant part. In the isobar and RPR models, the resonant part is composed of exchanges of nucleon resonances in the s channel that can model resonant phenomena in physical observables. The nonresonant part in an isobar model consists of the Born terms and exchanges of kaon resonances K^* and K_1 in the t channel and of hyperon resonances in the u channel. In kaon production, the contribution from the Born terms is very large and is reduced by assuming either hadronic form factors in the baryon-meson-baryon vertices [45] or additional exchanges of hyperon resonances in the u channel [38]. In the Gent isobar model, a combination of both methods is suggested [50]. The hadronic form factors suppress the

Born terms very strongly, especially at small kaon angles [51]. Selection of the method therefore considerably influences the dynamics of the isobar model. Besides the reduction of the Born terms, the hadronic form factors can model an internal structure of hadrons in the strong vertices that is neglected in the effective Lagrangian.

The problem of the Born contributions being too large is avoided in the RPR approach. In this model, the nonresonant part is composed of exchanges of two degenerate K and K^* trajectories. The three free parameters can be evaluated in fitting to photoproduction data above the resonance region [48]. Note that no hadronic form factors in the nonresonant part are needed. The different description of the nonresonant part is the main difference between the isobar and RPR models, which is important for very small kaon angles [36,51]; see also Sec. V A.

V. RESULTS

A. Elementary reaction

The elementary reaction, the Λ production mechanism, is fundamental to the interpretation of hypernuclear data [6–8]. The reaction has to be studied, especially at forward kaon angles ($\theta_K^{\text{c.m.}} < 30^\circ$), where there is a lack of data and a wide disagreement among existing models [34,36,37]. A realistic description of the elementary process at the forward angles is decisive for an accurate prediction of hypernuclear excitation spectra [34]. Measurements performed at very small values of the virtual-photon mass ($Q^2 \approx 0$) are important to the understanding of the process with virtual photons. In the framework of an effective Lagrangian, this means extending our knowledge about the couplings of the virtual photon with baryon fields (the longitudinal couplings) [36,39,52].

The study of $p(e, e'K^+)Y$ is important not only for the understanding of strangeness electroproduction but also for absolute missing-mass calibration of the spectrometer systems by using the well-known Λ and Σ^0 masses. Because of the lack of a neutron target, an absolute mass calibration with the hyperon production is impossible for the (K^-, π^-) or (π^+, K^+) reactions. Electroproduction at very forward angles ($\theta_K^{\text{c.m.}} < 10^\circ$) is important to provide reference data for isobar models that give inconsistent predictions of the forward-angle cross section, especially at the center-of-mass energies $W > 2$ GeV ($E_\gamma^{\text{lab}} > 1.7$ GeV), as shown for photoproduction in Refs. [34,36]. In Fig. 15, we show the predictions at $W = 2.21$ GeV of the Saclay-Lyon (SLA) [38], Williams-Ji-Cotanch (WJC) [46], Kaon-MAID (KM) [45], H2 [47], recent BS1 [35] and BS3 [39] isobar models, and of a fit RPR-1 [36] to recent data using the Regge-plus-resonance formalism by the Ghent group [48]. The elementary reaction has been studied during the E94-107 experiment, using a cryogenic target [53].

One goal of the current measurement was to determine the angular dependence of $d\sigma/d\Omega_K$ at very small angles. Photoproduction data from CLAS [54,58], SAPHIR [56], and LEPS [55] precisely constrain production models at larger angles ($\theta_K^{\text{c.m.}} > 30^\circ$), e.g., BS1, BS3, H2, and RPR-1 in Fig. 15 fitted to the CLAS data. However, available isobar [35,38,39,45–47] and Regge-plus-resonance [36,48] models vary widely at

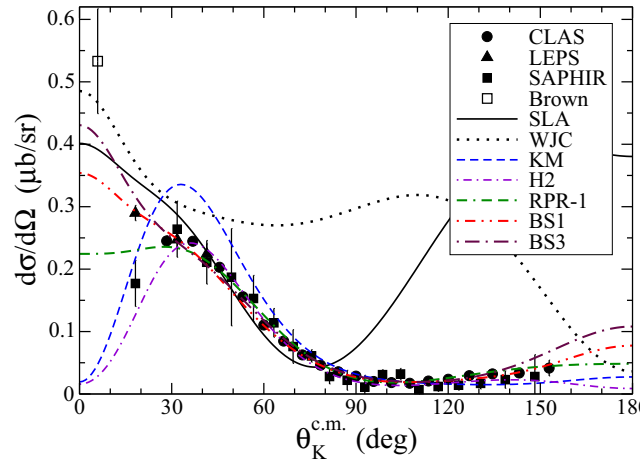

FIG. 15. Differential cross sections for photoproduction are plotted as a function of the center-of-mass angle at $W = 2.21$ GeV. Photoproduction data are from Refs. [54] (CLAS), [55] (LEPS), and [56] (SAPHIR). The electroproduction data "Brown" [57] is very near to the photoproduction point at $Q^2 = 0.18$ (GeV/c)^2 and $W = 2.17$ GeV. The larger angle data can constrain the curves but the utility of new small-angle results is evident.

$\theta_K^{\text{c.m.}} < 30^\circ$ (see Fig. 15) and the previous data are not adequate to choose between them. The current measurement provides data to constrain the angular dependence as θ_K goes to zero. A second goal was to measure the low Q^2 dependence of $d\sigma/d\Omega_K$ to determine a transition from photoproduction with real photons ($Q^2 = 0$) to the photoproduction induced by virtual photons [36,52]. The cross section at low Q^2 is also important for studies that want to extract the kaon form factor since we can compare to extrapolated measurements of the kaon charge radius.

Further, the data determine the Q^2 dependence of the Σ^0/Λ production ratio. This ratio drops off rapidly. In hadronic production, the ratio decreases from 10 at low energy to 3 by 1 GeV of energy transfer. In photoproduction, the ratio drops from 2 at 90 deg to 0.7 at 22 deg but data at forward angles have not been available. In electroproduction, the ratio for the transverse cross section drops from 0.7 at the photoproduction point to 0.1 at $Q^2 = 1$–2 (GeV/c)^2, but the behavior in between has not been determined. The longitudinal ratio is similar in magnitude to the transverse at nonzero Q^2. Whether this behavior is just due to isospin dependence in the Σ^0 and Λ couplings to resonances has not been known.

The E94-107 kinematics used beam energies of 4.016, 3.777, and 3.656 GeV. The corresponding electron momenta were p_e= 1.80, 1.57, and 1.44 GeV/c. The kaon momentum was centered $p_K = 1.96$ GeV/c for the hypernuclear running. For these hydrogen measurements, the beam energy was 3.777 GeV, p_e was 1.57 GeV/c, and p_K was 1.92, 1.96, and 2.0 GeV/c. The three kaon settings enabled us to slightly extend the range of kinematics as well as to move the missing-mass peak across the acceptance in a study of our understanding. These settings correspond to central values of $W = 2.2$ GeV and $Q^2 = 0.07$ (GeV/c)^2. This measurement used currents up of 60 μA on a 4-cm liquid hydrogen target. The

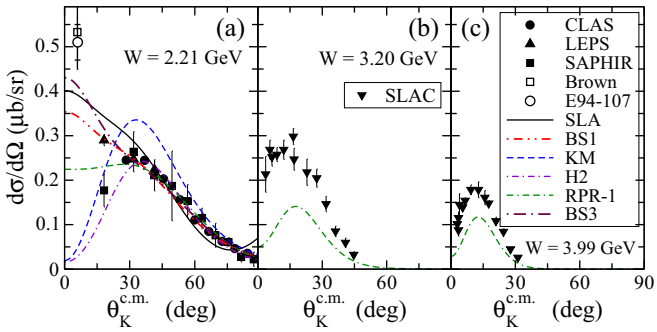

FIG. 16. The same as Fig. 15 but for three values of the center-of-mass energy. The result of this experiment (E94-107) is shown in part (a). The predictions of the Regge-plus-resonance model (RPR-1) [36] are comparred with SLAC data [59] above the resonance region in parts (b) and (c). The problem of normalization of the SLAC data is apparent.

analyzed data were compared to the standard Hall A Monte Carlo code, modified to incorporate the septum magnets. The comparison to the simulation was used to determine the acceptances and put cuts on the data to restrict the acceptance to a region where agreement between the shapes was excellent between simulation and acceptance.

The results are shown in Fig. 16(a). Plotted are the electroproduction results superimposed on the photoproduction data. Also shown are predictions for photoproduction of several models. As can be seen, results of the models markedly differ for kaon angles smaller than 30°. The relevant difference in dynamics of the presented models is in their description of the nonresonant part of the amplitude. The SLA isobar model does not assume any hadronic form factors but instead includes exchanges of hyperon resonances to suppress contributions from the Born terms (see also Sec. IV). The model KM includes hadronic form factors without any hyperon resonances and the H2, BS1, and BS3 models include both hyperon resonances and hadronic form factors. The strong suppression of the nonresonant part at very small angles is apparent when the hadronic form factors are used with or without a small number of hyperon resonances, as in the H2 and KM models, respectively. On the contrary, in the recent isobar models BS1 and BS3, an ample number of hyperon resonances with spin 1/2 and 3/2 contribute to the nonresonant part of the amplitude that results in a similar behavior of the cross section at $\theta_K^{\text{c.m.}} < 30^\circ$ as for the SLA model in Fig. 16(a). In the Regge-plus-resonance model RPR-1, the nonresonant part is given by the Regge trajectories without any hadronic form factors. The new results are therefore vital for understanding the dynamics of models at very small θ_K.

However, since the data (although at a low Q^2) are electroproduction not photoproduction, it is possible that the longitudinal amplitudes might strongly contribute to the cross section. We estimated the maximum contribution using the available data on longitudinal-transverse separations of the kaon cross sections. Independent of Q^2 and W, the data suggest a value of $\sigma_L/\sigma_T \approx 0.5$. For this experiment's kinematics, this would mean $\sigma_T \approx 0.38$ μb/sr. This value, that corresponds to the photoproduction cross section, rules out the models that predict a strong reduction of the cross section at small angles, e.g., KM and H2 in Fig. 16(a), and favor a steep angular dependence for near-zero angles predicted by the isobar SLA, BS1, and BS3 models and by the Regge models (see also Fig. 6 in Ref. [51]). Note that the SLA model gives the best predictions for the hypernuclear excitation functions [6–8], which implies that this model provides a realistic description of the elementary process at the very small angles that dominate hypernuclear production. The forward peaking of the cross section is also consistent with conclusions from the analysis of CLAS data [58]. The authors concluded that in the energy region $2.3 < W < 2.6$ GeV, with 2.6 GeV being the maximum energy in the experiment, the cross section is dominantly forward peaked, from which it can be inferred that a substantial contribution to the reaction mechanism comes from t-channel exchange. The Regge-plus-resonance model, RPR-1, predicts a plateau at small angles and energies about 2.2 GeV [Fig. 16(a)], showing that the Regge-based modeling of the nonresonant part of amplitude can also provide reasonable results in this kinematics.

In Figs. 16(b) and 16(c), we show the angular dependence above the resonance region at $W = 3.20$ GeV ($E_\gamma^{\text{lab}} = 5$ GeV) and 3.99 GeV ($E_\gamma^{\text{lab}} = 8$ GeV), respectively. The SLAC data [59] and predictions of the RPR-1 model are shown. First, note a problem with the normalization of the SLAC data [60] that, we suppose, will not significantly affect the angular dependence. In the higher energy region, $W > 3.2$ GeV, the SLAC data reveal an inverse angular dependence at very small kaon angles compared to that observed in the resonance region at $W = 2.21$ GeV by the present measurement and by Bradford *et al.* in Ref. [58]. Therefore, the SLAC data, if their angular dependence does not change in a reanalysis due to the normalization, suggest that the RPR-1 model gives a correct angular dependence at very small kaon angles over a large energy region, which means that at 2.2 GeV a flat angular dependence (plateau) is a more realistic behavior of the cross section. Note that some Regge-based models can predict also forward-peaking cross sections, in agreement with the present data but in disagreement with the SLAC data (see Fig. 6 in Ref. [51]). It is obvious that new good-quality experimental data for kaon c.m. angles 0–20° and in a broader energy region are needed to better understand the reaction mechanism.

The data were also rebinned in three Q^2 bins to determine the Q^2 slope. What is observed is that the differential cross section for Λ production drops with increasing Q^2, while the differential cross section for Σ^0 production is flat. A similar rebinning into three $\theta_K^{\text{c.m.}}$ bins is essentially flat for both Λ and Σ^0, ruling out any sharp drop with angle for the Λ production. The W rebinning data are also flat with energy, as expected from photoproduction at larger angles. The extracted Σ^0/Λ ratio is approximately 0.5 and flat with respect to the kinematics. Interestingly, this is similar to what the photoproduction data would give if extrapolated by a straight line.

B. Hypernuclear electroproduction

Results from the experiment E94-107 on hypernuclear electroproduction have been already published and briefly

discussed in Refs. [7] ($^{12}_{\Lambda}$B), [8] ($^{16}_{\Lambda}$N), and [6] ($^{9}_{\Lambda}$Li). Here, we present new radiative corrected results for $^{12}_{\Lambda}$B, similar to what was done for $^{9}_{\Lambda}$Li. The experimental results for all targets are compared here with new theoretical predictions based on improved reaction calculations in DWIA. The improvement consists mainly in using new structure calculations for the one-body density matrix elements, corrected kaon distortion, and taking into account hypernuclear-recoil effects. The latter consists in correcting the hypernuclear mass for the excitation energy that appears to have a considerable effect on the hypernuclear kinetic energy and, especially, for the production cross sections (a few percent). In our previous calculations, this was included only in the case of the oxygen target [8]. We also utilized a more realistic description of the single-particle states of the initial proton and final Λ by using Woods-Saxon wave functions. In comparison with our previous calculations in Refs. [6–8], we give here also results with the new isobar model BS3 [39]. The calculations are also compared with the data from the Hall C experiments E01-011 and E05-115 in Subsec. V C.

1. The ^{9}Be *target*

There are still some unresolved problems in the spectroscopy of hypernuclei in the lower part of the *p* shell. The spectra of $^{10}_{\Lambda}$B (ground-state doublet splitting) and $^{11}_{\Lambda}$B (energy of the $1/2^+$ member of the first-excited doublet), as studied in precise $(K^-, \pi^-\gamma)$ and $(\pi^+, K^+\gamma)$ experiments, are inconsistent with the standard shell-model description of *p*-shell hypernuclei [43]. The electroproduction of $^{9}_{\Lambda}$Li from a ^{9}Be target can hopefully shed new light on this problem. In this case, the ground-state doublet and two excited doublets of $^{9}_{\Lambda}$Li (all lying below the neutron-decay threshold) are produced with comparable cross sections. In addition, the splittings of the ground-state doublet and the second excited-state doublet are predicted to be large enough to be detected (≈500 keV), while the first excited-state doublet is predicted to be almost degenerate. Figure 1 of Ref. [6] shows the detailed shell-model predictions (see also Ref. [44]). Note that most of the proton removal strength for ^{9}Be is contained in the first three states of the ^{8}Li core. In addition, the p_Λ orbit is unbound at $A=9$ and there is no evidence for sharp p_Λ states in the $(e, e'K^+)$ spectrum [6].

Figure 17 shows the binding-energy spectrum for $^{9}_{\Lambda}$Li production and gives the radiative-corrected experimental data (the points with statistical errors) [6] versus the new theoretical results (dashed and dash-dotted lines) shifted by −0.34 MeV (see caption). The band at the bottom of the histogram shows the systematic errors. A more detailed description of the procedure employed to determine the radiative corrected spectrum can be found in Sec. III K and in Appendix A of Ref. [6].

Once radiative corrections are applied, the binding-energy resolution is small enough to clearly show a three-peak structure of the spectrum based on the lowest three states of ^{8}Li. The experimental spectrum in Fig. 17 was fitted, assuming two Gaussians for the ground-state doublet and two Gaussians for the second and third multiplets (solid line). The Gaussians were taken to have a common width that was determined to be

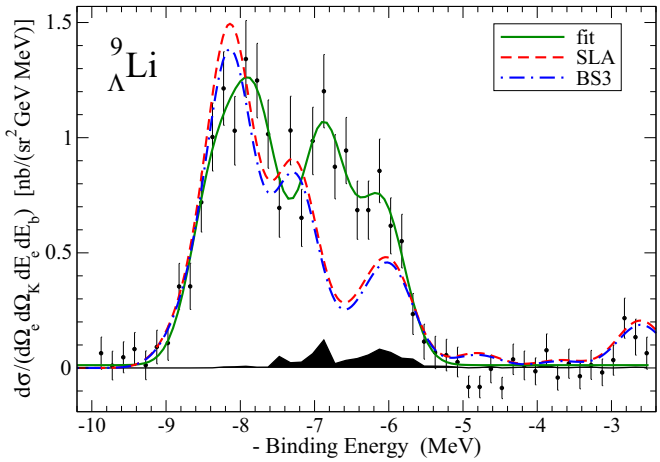

FIG. 17. The radiative-corrected experimental spectrum of $^{9}_{\Lambda}$Li in comparison with the theoretical prediction (dashed and dash-dotted lines). The solid line shows the result of fitting the data with four Gaussians of a common width. The theoretical curves were calculated with the width extracted from the fit (FWHM = 730 keV). Note that for a better comparison between theory and experiment, the theoretical curves have been shifted by −0.34 MeV with respect to the excitation energies given in Table II.

FWHM = 730 keV. A constant background was found to be negligible in the fit being 0.2% at maximum and the $\chi^2_{n.d.f}$ was 1.04. The theoretical curves were obtained by superposing Gaussians with an energy resolution of 730 keV (FWHM).

The cross sections were calculated using the complete *p*-shell basis for the core nucleus but with a slightly different interaction for the *p*-shell core from Ref. [6] that results, e.g., in the interchange of the second closely separated $1/2^+$-$3/2^+$ doublet but otherwise negligible changes. Moreover, we used realistic Woods-Saxon wave functions for the initial proton in the $p_{3/2}$ state bound by 16.89 MeV and the final Λ in the $s_{1/2}$ state bound by 8.53 MeV. Parameters of the kaon distortion were revised utilizing the separable model for *KN* scattering. The hypernuclear recoil was properly included even if in this case its effect is not as big as in the case of the other targets. The elementary reaction, $p(e, e'K^+)\Lambda$, was described using the Saclay-Lyon (SLA) [38] and BS3 [39] models.

The energies, widths, and cross sections extracted from the four-peak fit are reported in Table II where they are compared with the calculated results for the six lowest states of $^{9}_{\Lambda}$Li. The plot in Fig. 17 and Table II show some disagreement between the DWIA calculation with a standard model of *p*-shell hypernuclei and the measurements, both for the position of the peaks and for the cross sections. Specifically, the theory predicts a larger ratio of the cross sections for the members of the ground-state doublet than the data show. Likewise, the theory predicts a larger spacing between the second and third doublets than the data show. The $5/2^+$ state is predicted by both models to be dominantly populated because of the structural dominance of spin flip (see Fig. 1 of Ref. [6]) and the strong dominance of the spin-flip part of the elementary amplitude at very small production angles ($\theta_{K\gamma} = 1.8°$). The predicted theoretical cross sections are generally in better

TABLE II. Excitation energies, widths, and cross sections obtained by fitting the ^{9}Be$(e, e'K^+)^{9}_{\Lambda}$Li spectrum (first three columns) compared with theoretical predictions using the SLA and BS3 models for the elementary interaction (last four columns). Columns four and five give the E_x and J^π from the shell-model calculation. A summed cross section is given for each of the three doublets to compare with the experimental results in the third column.

Experimental data					Theoretical cross sections			
					SLA		BS3	
E_x (MeV)	Width (FWHM) (MeV)	Cross section [nb/(sr^{2}GeV)]	E_x (MeV)	J^π	[nb/(sr^{2}GeV)]	Sum	[nb/(sr^{2}GeV)]	Sum
0.00 ± 0.08	0.73 ± 0.06	0.59 ± 0.15	0.00	$3/2^+$	0.164		0.157	
0.57 ± 0.12	0.73 ± 0.06	0.83 ± 0.13	0.56	$5/2^+$	1.118	1.28	1.035	1.19
1.47 ± 0.09	0.73 ± 0.06	0.79 ± 0.07	1.42	$1/2^+$	0.353		0.294	
			1.45	$3/2^+$	0.327	0.68	0.343	0.64
2.27 ± 0.09	0.73 ± 0.06	0.54 ± 0.06	2.27	$5/2^+$	0.130		0.109	
			2.73	$7/2^+$	0.324	0.45	0.315	0.42

agreement with data than in Ref. [6] but they are still systematically 10–20% below the experimental values, which we attribute mainly to uncertainty in the elementary-production operator [34]. Note that the hypernuclear cross sections calculated with BS3 are, in general, smaller that those calculated with SLA contrary to a naive expectation from a comparison of the elementary cross sections in Fig. 16(a), where BS3 predicts larger values at $\theta_k < 10^\circ$ than SLA. This effect is due to a steeper descent of the transverse component as a function of Q^2 for BS3 compared with SLA.

It is worth noting that the structure calculations of doublet properties are generally in agreement with data [41,43,44]. There are disagreements for the spacing between doublets. These depend mainly on S_N and perhaps also on the three-body ΛNN interaction that has not yet been included in the shell-model calculations [43]. The cross sections depend on the spectroscopic factors for proton removal from the target. For the present case, a comparison between the p-shell calculations and pickup data was made in Ref. [6]. This strength gets redistributed somewhat in the hypernuclear shell-model calculation (see Fig. 1 of Ref. [6]).

2. *The* ^{12}C *target*

^{12}C targets have been extensively used in hypernuclear studies using (K^-, π^-), (π^+, K^+), and $(K^-_{\rm stop}, \pi^-)$ reactions dominated by non-spin-flip contributions. In the early experiments, only two peaks, separated by about 11 MeV and attributed to the Λ being in an s or p orbit coupled to the ^{11}C ground state, were evident [4]. The first evidence of structure between the main peaks came from (π^+, K^+) studies with the SKS spectrometer at KEK (E140a, E336, and E369) [4], with the best resolution of 1.45 MeV being obtained in KEK E369 [61]. Finally, in the stopped K^- experiment of the FINUDA Collaboration [62], further evidence for structure in this region has been observed. However, either because of relatively poor energy resolution or statistics, the extraction of energies and cross sections from peak fitting was difficult. The first electroproduction experiment performed on a ^{12}C target in Hall C [63] had limited statistics but proved that the electroproduction process can be used to study hypernuclear spectra with a sub-MeV energy resolution and measured cross sections. Further measurements in Hall C [64,65] show that a rich structure in the Λ-binding energy spectrum of $^{12}_{\Lambda}$B can be observed with a very good energy resolution and that hypernuclear reaction spectroscopy is possible.

The theoretical spectrum for $p^7 s_\Lambda$ and $p^7 p_\Lambda$ states of $^{12}_{\Lambda}$B using the Cohen and Kurath (8-16)2BME interaction [66] for the ^{11}B core states is shown in Fig. 18. The standard ps_Λ parameters for the heavier p-shell hypernuclei from Eq. (4) of Ref. [43] were used along with pp_Λ matrix elements calculated from a potential, called fit-djm in Ref. [43], using Woods-Saxon wave functions with a binding energy of 0.4 MeV for the loosely bound p_Λ orbits. The experimentally known states of interest for the ^{11}B core are shown on the left and structure factors for non-spin-flip and spin-flip transitions on the right. The latter give the relative population of states for the purely transverse spin operator in the $(e, e'K^+)$ reaction.

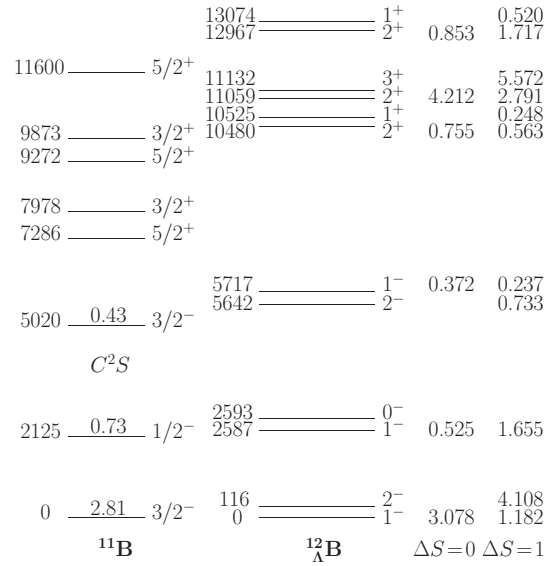

FIG. 18. The calculated spectrum of $^{12}_{\Lambda}$B. The ^{11}B core states are shown on the left along with the spectroscopic factors for proton removal from ^{12}C. All excitation energies are in keV. On the right, the factors giving the relative population of purely non-spin-flip ($\Delta S = 0$) and purely spin-flip ($\Delta S = 1$) production reactions on ^{12}C with $\Delta L = 1$ ($\pi = -$) or $\Delta L = 2$ ($\pi = +$) are given.

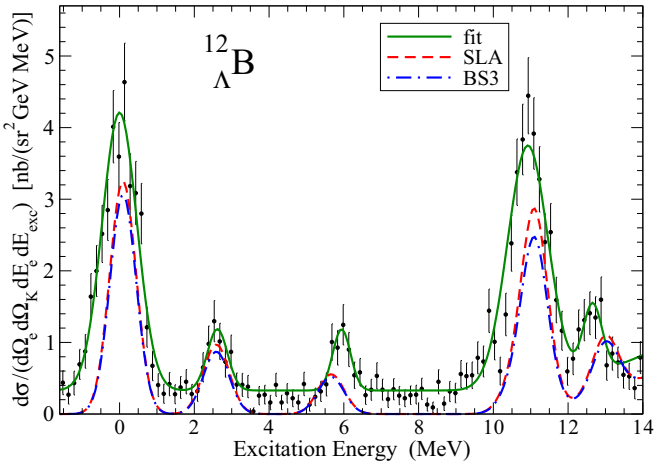

FIG. 19. The radiative-corrected experimental excitation-energy spectrum of $^{12}_{\Lambda}$B (the points with statistical errors) in comparison with the theoretical prediction (dashed and dash-dotted lines). The solid line shows the result of fits to the data with six Gaussians with independent widths. The theoretical curves were calculated with the average width extracted from the fit (FWHM = 820 keV) without any background.

The splitting of the ground-state doublet in $^{12}_{\Lambda}$C is known to be 161.5 keV from hypernuclear γ-ray spectroscopy while the excitation energies of the excited 1^- states are 2832 and 6050 keV [31]. The energies of the excited 1^- states should be a little higher in $^{12}_{\Lambda}$B and it is clear that the theoretically predicted excitation energies are more than 300 keV too low.

The p_Λ part of the spectrum should be dominated by the $2^+/3^+$ doublet near 11 MeV in Fig. 18 in electroproduction. The p_Λ doublets are characterized by the coupling of the Λ spin to L arising from the coupling of the core spin to the orbital angular momentum of the p_Λ [67]. Two $0^+/1^+$ doublets, that complete the multiplets of states built on the lowest $3/2^-$ and $1/2^-$ of ^{11}B, are not shown in Fig. 18. The lower one, with the 0^+ state at 11.197 MeV and the 1^+ state at 11.674 MeV, contains states that should be strongly excited by $\Delta L=0$ transitions from ^{12}C; the 0^+ state dominates the (K^-,π^-) spectrum at small angles [4]. The 2^+ states are excited in (π^+,K^+) reactions while the 2^+ states and the 0^+ state are excited in the $(K^-_{\rm stop},\pi^-)$ reaction.

Results of a new analysis of data from Hall A measurements [7] are presented in Fig. 19 that shows the radiatively unfolded excitation-energy spectrum for $^{12}_{\Lambda}$B as was done in the case of $^{9}_{\Lambda}$Li (the points with statistical errors). The spectrum was fitted assuming six Gaussians for the apparent structures (multiplets) with independent widths. The background was found to be constant up to the Λ separation energy at 11.37 MeV. Above this energy, a continuation of the constant background and a quadratic polynomial that mimics the quasifree Λ production process were used to fit the spectrum. A very good fit was obtained (solid line in Fig. 19) with $\chi^2_{n.d.f.} = 1.05$. The widths (FWHM) were obtained in the range of 650–1010 keV, where the widths of the two main peaks are similar at 990 and 1010 keV. A small peak at an excitation energy 9.59 MeV was added in the original analysis due to an apparent shoulder in this energy region. However, in a new analysis using the data from Ref. [7] but with radiative corrections, the statistical evidence for such a peak vanished. The origin of the excitation-energy scale was set to the peak value of the ground-state (g.s.) level (the uncertainty of the absolute scale being about 0.5 MeV). The energies, widths, and cross sections extracted from the six-peak fit are reported in Table III, where they are compared with the calculated results for lowest states of $^{12}_{\Lambda}$B. The theoretical curves in Fig. 19 (dashed and dash-dotted lines) were obtained using Gaussians with a width of 820 keV (FWHM) for the energy resolution. This width is consistent with values extracted from the fit.

The cross sections in Table III were calculated using new nucleus-hypernucleus structure constants for the p_Λ part of the spectrum calculated using one-body density-matrix elements from a new shell-model calculation including all p_Λ and p_Σ states. In comparison with the previous calculations in Ref. [7], the kaon-nucleus optical potential was improved and the momentum transfer included the correction for hypernucleus excitation energy. Realistic Woods-Saxon wave functions for the radial part of the proton and Λ wave functions were used also for the Λ s-state part of the spectrum. The protons in $p_{3/2}$ and $p_{1/2}$ states were taken to be bound by 15.96 and 10.37 MeV, respectively. The Λ in the s state was bound by 11.37 MeV and Λ in the p state by only 0.4 MeV. The elementary production was described by SLA as in Ref. [7] and by BS3 [39]. The comparison with the data shows that theory mostly underpredicts the cross sections by 20–40%, similarly to what it does in the case of $^{9}_{\Lambda}$Li. Smaller cross sections in comparison with our previous theoretical results in Ref. [7] are due to a stronger kaon distortion that, in general, makes the cross sections smaller.

Five peaks are observed in the spectrum of $^{12}_{\Lambda}$B, the main ones being the g.s. peak and the p-shell peak at 10.93 MeV. The narrowest width of 560 keV has been obtained for the peak at $E_x = 5.94$ MeV, indicating that the experimental energy resolution is below 1 MeV. The two main peaks, including the g.s., have widths larger than the above resolution suggesting that they are composed of two or more peaks separated by a noticeable excitation energy. Because of the very low level of background, states with an s_Λ coupled to excited ^{11}B core states are clearly observed between the g.s. and the level at 10.93 MeV with signal-to-noise ratios larger than 5. The positions of these levels were determined with uncertainties of less than 100 keV. Cross sections are determined at the level of 15–20%. As in the Hall C experiments [65], measurable strength has been observed with good energy resolution in this core-excited part of the spectrum. This is because the spin-spin interaction enhances the cross sections for these states with respect to the weak-coupling limit (compare the structure factors on the right in Fig. 18 with C^2S on the left).

3. The ^{16}O target

^{16}O targets have been extensively used in hypernuclear studies with the (K^-,π^-), (π^+,K^+), and $(K^-_{\rm stop},\pi^-)$ reactions with dominant non-spin-flip reaction mechanisms that

TABLE III. Excitation energies, widths, and cross sections obtained by fitting the ^{12}C$(e, e'K^+)^{12}_{\Lambda}$B spectrum (first three columns) compared with theoretical predictions using the SLA and BS3 models for the elementary interaction (last four columns). Columns four and five give the E_x and J^π from the shell-model calculation.

Experimental data					Theoretical cross sections			
E_x	Width (FWHM)	Cross section	E_x	J^π	SLA		BS3	
(MeV)	(MeV)	[nb/(sr^{2}GeV)]	(MeV)		[nb/(sr^{2}GeV)]	Sum	[nb/(sr^{2}GeV)]	Sum
0.00 ± 0.03	1.09 ± 0.05	$4.51 \pm 0.23 \pm 0.67$	0.00	1^-	0.640		0.524	
			0.116	2^-	2.227	2.87	2.172	2.70
2.62 ± 0.06	0.64 ± 0.11	$0.58 \pm 0.10 \pm 0.11$	2.587	1^-	0.846		0.689	
			2.593	0^-	0.001	0.85	0.071	0.76
5.94 ± 0.06	0.56 ± 0.10	$0.51 \pm 0.09 \pm 0.09$	5.642	2^-	0.368		0.359	
			5.717	1^-	0.119	0.49	0.097	0.46
10.93 ± 0.04	1.29 ± 0.07	$4.68 \pm 0.24 \pm 0.60$	10.480	2^+	0.194		0.157	
			10.525	1^+	0.085		0.100	
			11.059	2^+	0.959		0.778	
			11.132	3^+	1.485		1.324	
			11.674	1^+	0.050	2.77	0.047	2.41
12.65 ± 0.06	0.60 ± 0.11	$0.63 \pm 0.12 \pm 0.15$	12.967	2^+	0.552		0.447	
			13.074	1^+	0.167	0.72	0.196	0.64

excite natural-parity states [4]. In all cases, four peaks are seen with the excited states at ≈6.2, ≈10.6, and ≈17.1 MeV corresponding to Λ's in s and p orbits coupled to the $p^{-1}_{1/2}$ ground state and the 6.176-MeV $p^{-1}_{3/2}$ state of ^{15}O. In the simple particle-hole limit, the degenerate multiplets contain 2, 2, 4, and 6 states, respectively, and the cross sections would be in the ratio 2:1 for peaks based on the $p_{3/2}$ versus $p_{1/2}$ hole states. The first two peaks correspond to 1^- states and the B_Λ value for the lowest 1^- state is not particularly well determined. In the CERN (K^-, π^-) experiment [68], the third and fourth peaks correspond to substitutional 0^+ states. At the larger momentum transfer of the stopped K^- work at KEK [69], the same peaks contain contributions from both 0^+ and 2^+ hypernuclear states. In the (π^+, K^+) reaction, first performed at BNL [70] and later at KEK [4] with better energy resolution, only the 2^+ states are expected to contribute. Finally from γ-ray spectroscopy, the 0^- state in $^{16}_{\Lambda}$O is the ground state, the ground-state doublet spacing is 26.4 keV, and the 1^- and 2^- states of the excited doublet are at 6562 and 6786 keV, respectively [71]. The experimental knowledge can be enhanced using the $(e, e'K^+)$ electroproduction reaction characterized by a large momentum transfer to the hypernucleus ($q \gtrsim 250$ MeV/c) and strong spin-flip terms, even at zero-deg K^+ production angles, resulting in the excitation of both natural- and unnatural-parity states. In the present case, 1^-, 2^-, 1^+, 2^+, and 3^+ particle-hole states can be excited with significant cross sections. In addition, the $K^+\Lambda$ associated production occurs on a proton making $^{16}_{\Lambda}$N, the mirror to $^{16}_{\Lambda}$O. After taking into account that the $p_{3/2}$-hole state is 148 keV higher in ^{15}N than ^{15}O, comparison of the energy spectra (and especially of Λ binding energies) of these mirror hypernuclei can, in principle, shed light on charge-dependent effects in hyperon-nucleon interactions.

The binding-energy spectrum for $^{16}_{\Lambda}$N electroproduction is shown in Fig. 20, where the experimental data from this experiment (the points with statistical errors) [8] are compared with theoretical predictions (dashed and dash-dotted lines). The fit to the data (solid line) has been made using Voigt functions that in our case were the convolution of a narrow Gaussian with FWHM = 774 keV (from the fit) and the Breit-Wigner form of independent widths (to account for different residual radiative effects). Practically a zero constant background up to the quasifree threshold at 13.76 MeV and a $\chi^2_{n.d.f.} = 1.01$ were obtained. In the quasifree region, a quadratic form of background was assumed, similar to the

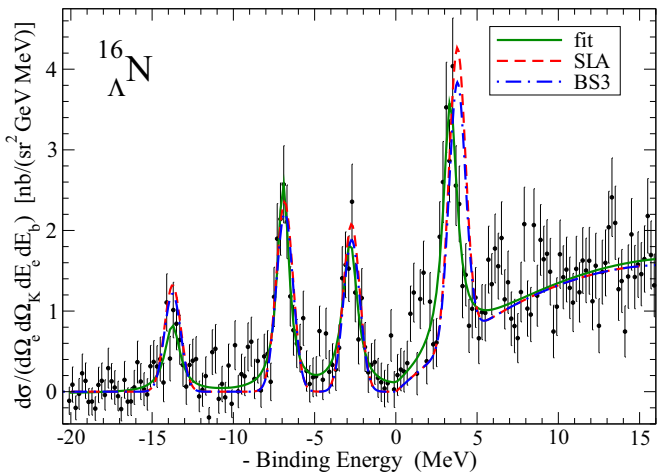

FIG. 20. The $^{16}_{\Lambda}$N binding-energy spectrum. The solid line shows the best fit using Voigt functions (see text for details). The theoretical curves (dashed and dash-dotted lines) were calculated with an average width extracted from the fit (FWHM = 1177 keV).

TABLE IV. Excitation energies, widths, and cross sections obtained by fitting the ^{16}O$(e, e'K^+)^{16}_{\Lambda}$N spectrum (first three columns) compared with theoretical predictions using the SLA and BS3 models for the elementary interaction (last four columns). Columns four and five give the E_x and J^π from the shell-model calculation.

Experimental data					Theoretical cross sections			
E_x	Width (FWHM)	Cross section	E_x	J^π	SLA		BS3	
(MeV)	(MeV)	[nb/(sr^{2}GeV)]	(MeV)		[nb/(sr^{2}GeV)]	Sum	[nb/(sr^{2}GeV)]	Sum
0.00 ± 0.02	1.71 ± 0.70	1.45 ± 0.26	0.000	0^-	0.003		0.134	
			0.023	1^-	1.657	1.66	1.391	1.52
6.83 ± 0.06	0.88 ± 0.31	3.16 ± 0.35	6.730	1^-	0.818		0.688	
			6.978	2^-	2.201	3.02	2.153	2.84
10.92 ± 0.07	0.99 ± 0.29	2.11 ± 0.37	11.000	2^+	1.948		1.627	
			11.116	1^+	0.607		0.679	
			11.249	1^+	0.069	2.62	0.071	2.38
17.10 ± 0.07	1.00 ± 0.23	3.44 ± 0.52	17.303	1^+	0.166		0.181	
			17.515	3^+	2.311		2.045	
			17.567	2^+	2.071	4.55	1.723	3.95

case of $^{12}_{\Lambda}$B. The FWHM around 1000 keV was obtained for all peaks consistent with the $^{12}_{\Lambda}$B case.

The values of excitation energies, widths, and cross sections extracted from the fit are given in Table IV together with the predicted cross sections for the lowest states of $^{16}_{\Lambda}$N (the structure comes from a simple particle-hole calculation). Only statistical errors are reported for the measured cross sections. Systematic errors, dominated by uncertainty in the target thickness, are at the 20% level. In the DWIA calculations, improved kaon distortion and better Woods-Saxon radial wave functions were used in comparison with our previous calculations [8]. In the old calculations, only the proton in $p_{1/2}$ state and also a stronger kaon absorption were considered where the latter had reduced the cross sections. In the new computation of the Woods-Saxon wave functions, the target proton was bound by 17.82 and 11.20 MeV for the $p_{3/2}$ and $p_{1/2}$ states, respectively and the final Λ was considered to be bound by 13.5, 2.3, and 2.9 MeV for the $s_{1/2}$, $p_{1/2}$, and $p_{3/2}$ states, respectively.

Four peaks are observed in the spectrum. The ground-state peak gives a Λ separation energy of $B_\Lambda = 13.76 \pm 0.16\,(\text{stat.}) \pm 0.04\,(\text{syst.})$ MeV ($\approx \pm 0.16$ MeV, adding statistical and systematic errors in quadrature) for the 1^- member of the ground-state doublet in $^{16}_{\Lambda}$N (that is at an excitation energy of 26 keV [71]). Three more peaks are observed at binding energies of 6.93, 2.84, and -3.34 MeV. The theory overpredicts the cross sections by 10–30%, contrary to the case of $^{12}_{\Lambda}$B and $^{9}_{\Lambda}$Li production. This opposite tendency of the hypernuclear cross sections can be hardly attributed to uncertainty in the elementary production cross sections [34,37]. The overpredicted cross section is more likely due the use of simple hole states for the ^{15}N core nucleus because the analysis of the ^{16}O$(e, e'p)^{15}$N reaction shows that the spectroscopic factors for proton removal are reduced from their simple shell-model values and that the discrete $3/2^-$ strength is spread over four states [72], a fact that has to be explained by a multi-$\hbar\omega$ shell-model calculation. This argument does not work to explain the underpredicted cross section for the ^{12}C target because a similar analysis of the $(e, e'p)$ reaction in this case again shows the usual reduction in spectroscopic factors with respect to p-shell values [73].

C. Hall C data

To compare our theoretical results for $^{12}_{\Lambda}$B production with data from the Hall C experiments E01-011 and E05-115 [65], we use the kinematics presented in Table V for the values of E_i, E_f, θ_e, θ_{Ke}, and $\Phi_K = 90^\circ$. Note that the virtual-photon energy and mass (Q^2) and the kaon momentum significantly differ in the Hall A and C measurements; see Tables I and V.

The results are presented in Table VI. As in Table III for the Hall A experiment, the theoretical cross sections are 30–50% smaller than the experimental values, suggesting that this phenomenon is present in a broader beam-energy region. In Table VI, we make assignments with certainty only for the Λ s-wave states and leave open an assignment for the higher states.

TABLE V. Central kinematics of the Hall C experiments with the carbon target in the laboratory reference frame. The values of E_i, E_f, θ_e, θ_{Ke}, and $\Phi_K = 90^\circ$ were used in our calculations.

Experiment	E_i (GeV)	E_f (GeV)	θ_e (deg)	θ_{Ke} (deg)	E_γ (GeV)	$\theta_{\gamma e}$ (deg)	Q^2 (GeV^2)	ϵ	Γ [(GeV sr)$^{-1}$]	p_K (GeV)
E01-011	1.851	0.351	5.4	7.11	1.50	1.26	0.00577	0.365	0.0287	1.20–1.22
E05-115	2.344	0.844	5.4	7.62	1.50	3.02	0.01756	0.635	0.0310	1.20–1.22

TABLE VI. Comparison of theoretical predictions using the SLA and BS3 models for the elementary cross section for the two-folded cross sections in $^{12}\mathrm{C}(e,e'K^+)^{12}_{\Lambda}\mathrm{B}$ (last four columns) with data from the Hall C experiments [65] (first four columns). Columns five and six give the E_x and J^π from the shell-model calculation. The excitation energy was determined to be $11.517 - B_\Lambda$ MeV in E01-011 and $11.529 - B_\Lambda$ MeV in E05-115, where B_Λ is the Λ binding energy. The 8th and 10th columns give the summed cross section for the assigned multiplets, to compare with the experimental result in the fourth column.

Experimental data						Theoretical cross sections			
Peak	B_Λ	E_x	Cross section	E_x	J^π	SLA		BS3	
No.	(MeV)	(MeV)	(nb/sr)	(MeV)		(nb/sr)	Sum	(nb/sr)	Sum
				Experiment E01-011					
1	11.517 ± 0.031	0.0	101.0 ± 4.2	0.0	1^-	13.90		14.04	
				0.116	2^-	44.70	58.60	35.33	49.37
2	8.390 ± 0.075	3.127	33.5 ± 11.3	2.587	1^-	17.26		14.65	
				2.593	0^-	0.04	17.31	0.12	14.76
3	5.440 ± 0.085	6.077	26.0 ± 8.8	4.761	2^-	0.37		0.30	
				5.642	2^-	7.20		5.69	
				5.717	1^-	2.44	10.01	2.24	8.22
4	2.882 ± 0.085	8.635	20.5 ± 7.3						
5	1.470 ± 0.091	10.047	31.5 ± 7.4	10.480	2^+	5.15		5.16	
				10.525	1^+	2.16	7.31	1.77	6.93
6	0.548 ± 0.035	10.969	87.7 ± 15.4	11.059	2^+	25.23		22.35	
				11.132	3^+	39.08		29.70	
				11.197	0^+	0.10	64.41	0.42	52.47
7	-0.318 ± 0.085	11.835	46.3 ± 10.3	11.674	1^+	5.37	5.37	4.25	4.25
8	-0.849 ± 0.101	12.366	28.5 ± 7.4	12.967	2^+	13.96		12.37	
				13.074	1^+	4.36	18.32	3.57	15.93
				Experiment E05-115					
1	11.529 ± 0.025	0.0	83.0 ± 3.0	0.0	1^-	13.14		13.53	
				0.116	2^-	42.05	55.19	33.49	47.02
2	8.425 ± 0.047	3.104	19.1 ± 3.7	2.587	1^-	16.24		13.62	
				2.593	0^-	0.07	16.31	0.35	13.98
3	5.488 ± 0.052	6.041	18.0 ± 4.6	4.761	2^-	0.35		0.28	
				5.642	2^-	6.76		5.39	
				5.717	1^-	2.29	9.40	2.11	7.78
4	2.499 ± 0.075	9.030	16.2 ± 5.1						
5	1.220 ± 0.056	10.309	28.7 ± 7.2	10.480	2^+	4.90		4.98	
				10.525	1^+	2.07	6.97	1.78	6.77
6	0.524 ± 0.024	11.005	75.7 ± 10.8	11.059	2^+	23.97		21.24	
				11.132	3^+	41.17		32.40	
				11.197	0^+	0.12	65.26	0.49	54.12
7	-0.223 ± 0.039	11.752	39.0 ± 7.4	11.674	1^+	5.45	5.45	4.32	4.32
8	-1.047 ± 0.078	12.576	27.8 ± 7.9	12.967	2^+	13.25		11.69	
				13.074	1^+	4.18	17.44	3.57	15.27

Note that especially for E01-011 kinematics with very small Q^2, given in Table V, the cross section is dominated by the transverse contributions and therefore photoproduction calculations [34,74] are justified. Here, for the photon laboratory energy 1.5 GeV, the SLA model gives larger elementary cross sections than BS3 (see Fig. 5 in Ref. [39]) and therefore the hypernuclear cross sections are again larger for SLA than for BS3 as in the case of Hall A kinematics. We recall that in the Hall A case, smaller predictions of BS3 were due to steeper descent of the transverse elementary cross section with Q^2.

Finally, the Hall C fit to their data included five peaks in the region defined by $\approx$2 MeV on either side of the dominant p_Λ peak. Such peaks are not unexpected because states with an s_Λ coupled to the $3/2^+$ and $5/2^+$ core states shown at the left of Fig. 18 exist and can mix with the $p^7 p_\Lambda$ states and acquire some formation strength. These two types of states are both $1\hbar\omega$ states and one must eliminate spurious linear combinations from the full $1\hbar\omega$ shell-model basis [74] and this, by itself, enforces mixtures of the s_Λ and p_Λ states.

VI. SUMMARY AND CONCLUSIONS

The systematic study of hypernuclear spectroscopy by electroproduction of strangeness performed at Jefferson Laboratory in Hall A has been very successful. It has provided important elements for a better understanding of the baryon-baryon interactions and production mechanism in strangeness

physics. The experiment was successful but challenging because important modifications to the Hall A apparatus were needed. The new experimental equipment, aerogel threshold detectors, septum magnets, and the RICH detector all gave excellent performance. Sub-MeV energy resolution and very clean, background-free spectra were obtained. The results of the hypernuclear spectroscopy performed on ^{12}C, ^{16}O, and ^{9}Be targets provide important data for a better understanding of strangeness physics. Results from ^{12}C showed significant strength in the core-excited part of the spectrum. The spectrum is quite well reproduced by the theory apart from an overall underestimation of the experimental cross section. Moreover, for ^{16}O, thanks to the calibration with the hydrogen present in the waterfall target, a very precise determination of the Λ binding energy for $^{16}_{\Lambda}$N was obtained. In the case of ^{9}Be, the measured cross sections are in good agreement for the first peak with the values predicted using the SLA model and simple shell-model wave function. The reason for the disagreement in strength for the second and third peaks is hard to ascertain and could be due to a number of deficiences in the structure or reaction calculations.

We now list the improvements that have been made with respect to our previous separate publications on the data from the ^{12}C [7], ^{16}O [8], and ^{9}Be [6] targets:

(1) A new data point on the elementary electroproduction reaction at the forward-angle kinematics of the E94-107 experiment is presented. Given the lack of electroproduction data at the forward angles important for hypernuclear electroproduction, this is an important measurement. A detailed comparison of existing data on the elementary reaction (mostly photoproduction) with a wide range of models is presented.
(2) For the hypernuclear electroproduction, results from the BS3 isobar model are given for comparison with the SLA model used previously.
(3) A new analysis of the carbon data was made in which radiative corrections were performed as for the Be target. The spectrum was improved and the extracted peak widths are more consistent now.
(4) New structure and reaction calculations for carbon have been made that use the complete set of *p*-shell core states in the structure calculations, improved kaon distortion, include hypernuclear recoil, and use realistic Woods-Saxon wave functions.
(5) The theory (consistent calculations) was compared with data for several targets (Be, C, O) and for the carbon target for the different kinematics of Hall A and C experiments. This implies a test of the reaction mechanism for DWIA calculations.
(6) New calculations were made for the beryllium target. We used a new structure (fit4), improved kaon distortion, Woods-Saxon wave functions, and included the hypernuclear recoil.
(7) Slightly improved calculations were made for the oxygen target, using improved kaon distortion and using refined Woods-Saon wave functions.

In conclusion, we can also say that a more detailed analysis of the DWIA calculations using different elementary production amplitudes and larger basis shell-model calculations would be interesting (mainly due to our findings on the opposite discrepancies in cross sections for the ^{12}C and ^{16}O targets).

ACKNOWLEDGMENTS

We acknowledge the Jefferson Lab Physics and Accelerator Division staff for their outstanding efforts that made this work possible. We would like to single out the contributions made by our deceased colleagues Salvatore Frullani (significant contributions from the beginning of this project), Francesco Cusanno (leader of the analysis for the oxygen target), and Miloslav Sotona (reaction calculations for the three published papers). This work was supported by U.S. DOE Contract No. DE-AC05-06OR23177, under which the Southeastern Universities Research Association (SURA) operates the Thomas Jefferson National Accelerator Facility; the Italian Istituto Nazionale di Fisica Nucleare; the Grant Agency of the Czech Republic under Grant No. P203/15/04301; the French CEA and CNRS/IN2P3; the U.S. DOE under Contracts No. DE-AC02-06CH11357, No. DE-FG02-99ER41110, and No. DE-AC02-98-CH10886; and the U.S. National Science Foundation.

[1] A. Gal, E. V. Hungerford, and D. J. Millener, Strangeness in nuclear physics, Rev. Mod. Phys. **88**, 035004 (2016).
[2] *Hypernuclei and Baryon-Baryon Interaction*, edited by E. Hiyama, T. Motoba, and Y. Yamamoto, Prog. Theor. Phys. Suppl. No. 185 (2010).
[3] D. Lonardoni, S. Gandolfi, and F. Pederiva, Effects of the two-body and three-body hyperon-nucleon interactions in Λ-hypernuclei, Phys. Rev. C **87**, 041303(R) (2013).
[4] O. Hashimoto and H. Tamura, Spectroscopy of Λ hypernuclei, Prog. Part. Nucl. Phys. **57**, 564 (2006).
[5] F. Garibaldi, S. Frullani, P. Markowitz, and J. LeRose (spokespersons), JLab Experiment E94-107, high-resolution 1p shell hypernuclear spectroscopy (1994), https://www.jlab.org/exp_prog/proposals/94prop.html.
[6] G. M. Urciuoli, F. Cusanno, S. Marrone, A. Acha, P. Ambrozewicz, K. A. Aniol, P. Baturin, P. Y. Bertin, H. Benaoum, K. I. Blomqvist *et al.* (Jefferson Lab Hall A Collaboration), Spectroscopy of $^{9}_{\Lambda}$Li by electroproduction, Phys. Rev. C **91**, 034308 (2015).
[7] M. Iodice, F. Cusanno, A. Acha, P. Ambrozewicz, K. A. Aniol, P. Baturin, P. Y. Bertin, H. Benaoum, K. I. Blomqvist, W. U. Boeglin *et al.* (Jefferson Lab Hall A Collaboration), High-Resolution Spectroscopy of $^{12}_{\Lambda}$B by Electroproduction, Phys. Rev. Lett. **99**, 052501 (2007).

[8] F. Cusanno, G. M. Urciuoli, A. Acha, P. Ambrozewicz, K. A. Aniol, P. Baturin, P. Y. Bertin, H. Benaoum, K. I. Blomqvist, W. U. Boeglin *et al.* (Jefferson Lab Hall A Collaboration), High-Resolution Spectroscopy of $^{16}_{\Lambda}$N by Electroproduction, Phys. Rev. Lett. **103**, 202501 (2009).

[9] J. Alcorn, B. D. Anderson, K. A. Aniol, J. R. M. Annand, L. Auerbach, J. Arrington, T. Averett, F. T. Baker, M. Baylac, E. J. Beise *et al.*, Basic instrumentation for Hall A at Jefferson Lab, Nucl. Instrum. Methods Phys. Res., Sect. A **522**, 294 (2004).

[10] W. C. Barry, J. W. Heefner, G. S. Jones, J. E. Perry, and R. Rosssmanith, Beam position measurement in the CEBAF recirculating linacs by use of pseudorandom pulse sequences, JLab-TN-90-246, Jefferson Laboratory, Newport News, VA, 1990.

[11] W. Barry, Basic noise considerations for CEBAF beam position monitors, JLab-TN-91-087, Jefferson Laboratory, Newport News, VA, 1991.

[12] Y.-C. Chao, P. Chevtsov, A. Day, A. P. Freyberger, R. Hicks, M. Joyce, and J.-C. Denard, Energy spread monitoring for the JLAB experimental program: Synchrotron light interferometers, optical transition radiation monitors and wire scanners, in *Beam Instrumentation Workshop 2004*, edited by T. Shea and R. Coles Sibley III, AIP Conf. Proc. No. 732 (AIP, New York, 2004), p. 120.

[13] G. A. Krafft, J.-C. Denard, R. W. Dickson, R. Kazimi, V. A. Lebedev, and M. G. Tiefenback, Measuring and controlling the energy spread in CEBAF, in *Proceedings of the XX International Linac Conference, Monterey, California, USA*, SLAC-R-561, eConf:C000821 edited by A. W. Chao (Stanford Linear Accelerator Center, Stanford, California, 2000), p. 721.

[14] P. Chevtsov, A. Freyberger, R. Hicks, and J.-C. Denard, Synchrotron light interferometer at Jefferson Lab, in *Proceedings of 2003 Particle Accelerator Conference, Portland, Oregon, USA* (IEEE, New York, 2003), p. 2560.

[15] G. M. Urciuoli, P. Brindza, P. Bydžovský, C. C. Chang, E. Cisbani, F. Cusanno, R. De Leo, S. Frullani, F. Garibaldi, M. Iodice, L. Lagamba, S. Lassiter, J. J. Le Rose, P. Markowitz, and M. Sotona, Electroproduction of hypernuclei: An experimental challenge, Nucl. Phys. A **691**, 43c (2001).

[16] F. Garibaldi, E. Cisbani, R. Crateri, S. Frullani, F. Ghio, F. Giuliani, M. Gricia, M. Iodice, M. Lucentini, L. Pierangeli *et al.*, A waterfall target for electron scattering experiments, Nucl. Instrum. Methods Phys. Res., Sect. A **314**, 1 (1992).

[17] N. Voegler and J. Friedrich, A background-free oxygen target for electron scattering measurements with high beam currents, Nucl. Instrum. Methods **198**, 293 (1982).

[18] K. G. Fissum, W. Bertozzi, J. P. Chen, D. Dale, H. C. Fenker, J. Gao, A. Gavalya, S. Gilad, C. R. Leathers, N. Liyanage, R. O. Michaels, E. A. J. M. Offermann, J. Segal, J. A. Templon, R. Wechsler, B. Wojtsekhowski, and J. Zhao, Vertical drift chambers for the Hall A high-resolution spectrometers at Jefferson Lab, Nucl. Instrum. Methods Phys. Res., Sect. A **474**, 108 (2001).

[19] J. J. LeRose, Report on studies of the effect of resolution of the exit window of the HRS spectrometers in Hall A, JLab-TN-00-001, Jefferson Laboratory, Newport News, VA, 2000.

[20] M. Iodice, E. Cisbani, S. Colilli, R. Crateri, S. Frullani, F. Garibaldi, F. Giuliani, M. Gricia, M. Lucentinia, A. Mostardaa *et al.*, The CO_2 gas cherenkov detectors for the Jefferson Lab Hall-A spectrometers, Nucl. Instrum. Methods Phys. Res., Sect. A **411**, 223 (1998).

[21] E. Cisbani, S. Colilli, R. Crateri, F. Cusanno, R. Fratoni, S. Frullani, F. Garibaldi, F. Giuliani, M. Gricia, M. Iodice *et al.*, Light-weight spherical mirrors for Cherenkov detectors, Nucl. Instrum. Methods Phys. Res., Sect. A **496**, 305 (2003).

[22] L. Lagamba, E. Cisbani, S. Colilli, R. Crateri, R. De Leo, S. Frullani, F. Garibaldi, F. Giuliani, M. Gricia, M. Iodice *et al.*, Silica aerogel threshold Cherenkov counters for the JLab Hall A spectrometers: Improvements and proposed modifications, Nucl. Instrum. Methods Phys. Res., Sect. A **471**, 325 (2001).

[23] Detector for high momemntum PID, Technical design report of the ALICE HMPID detector, CERN/LHCC 98-19, ALICE TRD 1, 14 August 1998, http://alicehmpid.web.cern.ch/alice-hmpid/.

[24] M. Iodice, E. Cisbani, S. Colilli, F. Cusanno, S. Frullani, R. Fratoni, F. Garibaldi, M. Gricia, M. Lucentini, L. Pierangeli *et al.*, Performance and results of the RICH detector for kaon physics in Hall A at Jefferson Lab, Nucl. Instrum. Methods Phys. Res., Sect. A **553**, 231 (2005).

[25] F. Garibaldi, E. Cisbani, S. Colilli, F. Cusanno, S. Frullani, R. Fratoni, F. Giuliani, M. Gricia, M. Iodice, M. Lucentini *et al.*, A proximity focusing RICH detector for kaon physics at Jefferson Lab Hall A, Nucl. Instrum. Methods Phys. Res., Sect. A **502**, 117 (2003).

[26] F. Cusanno, E. Cisbani, S. Colilli, R. Crateri, R. Fratoni, S. Frullani, F. Garibaldi, F. Giuliani, M. Gricia, M. Lucentini *et al.*, Quantum efficiency measurement system for large area CsI photodetectors, Nucl. Instrum. Methods Phys. Res., Sect. A **502**, 251 (2003).

[27] F. Cusanno, High resolution hypernuclear spectroscopy at Jefferson Lab, Hall A, Ph.D. thesis, Roma Tre University, Rome, Italy, 2005 (unpublished).

[28] G. M. Urciuoli, E. Cisbani, F. Cusanno, R. De Leo, D. Di Bari, S. Frullani, F. Garibaldi, M. Iodice, L. Lagamba, J. J. LeRose, P. Markowitz, S. Marrone, and B. Reitz, A χ^2 test used for particle identification with the Hall A RICH, Nucl. Instrum. Methods Phys. Res., Sect. A **612**, 56 (2009).

[29] D. Gaskell and J. Arrington, SIMC-physics Monte Carlo for Hall C and Hall A https://hallaweb.jlab.org/data_reduc/AnaWork2009/simc_overview.pdf.

[30] G. M. Urciuoli *et al.* (unpublished).

[31] K. Hosomi, Y. Ma, S. Ajimura, K. Aoki, S. Dairaku, Y. Fu, H. Fujioka, K. Futatsukawa, W. Imoto, Y. Kakiguchi *et al.*, Precise determination of $^{12}_{\Lambda}$C level structure by γ-ray spectroscopy, Prog. Theor. Exp. Phys. **2015**, 081D01 (2015).

[32] M. Sotona and S. Frullani, Electroproduction of strangeness and spectroscopy of light hypernuclei, Prog. Theor. Phys. Suppl. **117**, 151 (1994).

[33] P. Bydžovský and M. Sotona, Separable model for K^+-nucleon scattering, in *Proceedings of the Seventh Conference on Mesons and Light Nuclei*, edited by J. Adam, P. Bydžovský, J. Dobes, R. Mach, J. Mareš, and M. Sotona (World Scientific, Singapore, 1999), p. 138.

[34] P. Bydžovský, M. Sotona, T. Motoba, K. Ogawa, and O. Hashimoto, Electromagnetic production of medium-mass Λ-hypernuclei, Nucl. Phys. A **881**, 199 (2012).

[35] D. Skoupil and P. Bydžovský, Photoproduction of $K\Lambda$ on the proton, Phys. Rev. C **93**, 025204 (2016).

[36] P. Bydžovský and D. Skoupil, Electromagnetic production of hyperons, Nucl. Phys. A **914**, 14 (2013).

[37] P. Bydžovský and T. Mart, Analysis of the consistency of kaon photoproduction data with Λ in the final state, Phys. Rev. C **76**, 065202 (2007).

[38] T. Mizutani, C. Fayard, G.-H. Lamot, and B. Saghai, Off-shell effects in the electromagnetic production of strangeness, Phys. Rev. C **58**, 75 (1998).

[39] D. Skoupil and P. Bydžovský, Photo- and electroproduction of $K^+\Lambda$ with a unitarity-restored isobar model, Phys. Rev. C **97**, 025202 (2018).

[40] M. Coman, P. Markowitz, K. A. Aniol, K. Baker, W. U. Boeglin, H. Breuer, P. Bydzovsky, A. Camsonne, J. Cha, C. C. Chang *et al.* (Jefferson Lab Hall A Collaboration), Cross sections and Rosenbluth separations in ^{1}H$(e, e'K^+)\Lambda$ up to $Q^2 = 2.35$ GeV^2, Phys. Rev. C **81**, 052201(R) (2010).

[41] D. J. Millener, Shell-model interpretation of γ-ray transitions in p-shell hypernuclei, Nucl. Phys. A **804**, 84 (2008).

[42] A. Gal, J. M. Soper, and R. H. Dalitz, A shell-model analysis of Λ binding energies for the p-shell hypernuclei, Ann. Phys. (NY) **63**, 53 (1971).

[43] D. J. Millener, Shell-model structure of light hypernuclei, Nucl. Phys. A **835**, 11 (2010).

[44] D. J. Millener, Shell-model calculations for p-shell hypernuclei, Nucl. Phys. A **881**, 298 (2012).

[45] T. Mart, C. Bennhold, H. Haberzettl, and L. Tiator https://maid.kph.uni-mainz.de/kaon.

[46] R. A. Williams, C. R. Ji, and S. R. Cotanch, Hyperon electroproduction in a crossing and duality constrained model, Phys. Rev. C **46**, 1617 (1992).

[47] P. Bydžovský and M. Sotona, Kaon electromagnetic production: Constraints set by new data, Nucl. Phys. A **754**, 243c (2005).

[48] L. De Cruz, T. Vrancx, P. Vancraeyveld, and J. Ryckebusch, Bayesian Inference of the Resonance Content of $p(\gamma, K^+)\Lambda$, Phys. Rev. Lett. **108**, 182002 (2012).

[49] M. Guidal, J.-M. Laget, and M. Vanderhaeghen, Pion and kaon photoproduction at high energies: Forward and intermediate angles, Nucl. Phys. A **627**, 645 (1997).

[50] S. Janssen, J. Ryckebusch, D. Debruyne, and T. Van Cauteren, Kaon photoproduction: Background contributions, form factors, and missing resonances, Phys. Rev. C **65**, 015201 (2001).

[51] P. Bydžovský and D. Skoupil, Present status of isobar models for elementary kaon photoproduction, in *International Workshop on Strangeness Nuclear Physics (SNP12), August 27-29, 2012, Neyagawa, Osaka, Japan*, edited by T. Fukuda, T. Harada, E. Hiyama, Y. Mizoi, T. Motoba, and H. Noumi, Vol. 57 (Genshikaku Kenkyu, 2013), pp. 86–92, arXiv:1211.2684.

[52] P. Achenbach, C. Ayerbe Gayoso, J. C. Bernauer, S. Bianchin, R. Böhm, O. Borodina, D. Bosnar, M. Bösz, V. Bozkurt, P. Bydzovsky *et al.* (A1 Collaboration), Exclusive electroproduction of $K^+\Lambda$ and $K^+\Sigma^0$ final states at $Q^2 = 0.030 - 0.055$ (GeV/c)^2, Eur. Phys. J. A **48**, 14 (2012).

[53] P. Markowitz and A. Acha, Low Q^2 kaon electroproduction, Int. J. Mod. Phys. E **19**, 2383 (2010).

[54] M. E. McCracken, M. Bellis, C. A. Meyer, M. Williams, K. P. Adhikari, M. Anghinolfi, J. Ball, M. Battaglieri, B. L. Berman, A. S. Biselli *et al.* (CLAS Collaboration), Differential cross section and recoil polarization measurements for the $\gamma p \to K^+\Lambda$ reaction using CLAS at Jefferson Lab, Phys. Rev. C **81**, 025201 (2010).

[55] M. Sumihama, J. K. Ahn, H. Akimune, Y. Asano, C. Bennhold, W. C. Chang, T. Corthals, S. Daté, H. Ejiri, H. Fujimura *et al.* (LEPS Collaboration), The $\vec{\gamma} p \to K^+\Lambda$ and $\vec{\gamma} p \to K^+\Sigma^0$ reactions at forward angles with photon energies from 1.5 to 2.4 GeV, Phys. Rev. C **73**, 035214 (2006).

[56] K.-H. Glander, J. Barth, W. Braun, J. Hannappel, N. Jöpen, F. Klein, E. Klempt, R. Lawall, J. Link, D. Menze *et al.* (SAPHIR Collaboration), Measurement of $\gamma p \to K^+\Lambda$ and $\gamma p \to K^+\Sigma^0$ at photon energies up to 2.6 GeV, Eur. Phys. J. A **19**, 251 (2004).

[57] C. N. Brown, C. R. Canizares, W. E. Cooper, A. M. Eisner, G. J. Feldman, C. A. Lichtenstein, L. Litt, W. Lockeretz, V. B. Montana, F. M. Pipkin, and N. Hicks, Coincidence Measurements of Single K^+ Electroproduction, Phys. Rev. Lett. **28**, 1086 (1972).

[58] R. Bradford, R. A. Schumacher, J. W. C. McNabb, L. Todor, G. Adams, P. Ambrozewicz, E. Anciant, M. Anghinolfi, B. Asavapibhop, G. Asryan *et al.* (CLAS Collaboration), Differential cross sections for $\gamma + p \to K^+ + Y$ for Λ and Σ^0 hyperons, Phys. Rev. C **73**, 035202 (2006).

[59] A. M. Boyarski, F. Bulos, W. Busza, R. Diebold, S. D. Ecklund, G. E. Fischer, Y. Murata, J. R. Rees, B. Richter, and W. S. C. Williams (SLAC Collaboration), Photoproduction of $K^+\Lambda$ and $K^+\Sigma^0$ from Hydrogen from 5 to 16 GeV, Phys. Rev. Lett. **22**, 1131 (1969).

[60] B. Dey and C. A. Meyer, Normalization discrepancies in photoproduction reactions, arXiv:1106.0479.

[61] H. Hotchi, T. Nagae, H. Outa, H. Noumi, M. Sekimoto, T. Fukuda, H. Bhang, Y. D. Kim, J. H. Kim, H. Park *et al.*, Spectroscopy of medium-heavy Λ hypernuclei via the (π^+, K^+) reaction, Phys. Rev. C **64**, 044302 (2001).

[62] M. Agnello, G. Beer, L. Benussi, M. Bertani, H. C. Bhang, S. Bianco, E. Botta, M. Bregant, T. Bressani, L. Busso *et al.* (FINUDA Collaboration), First results on $^{12}_{\Lambda}$C production at DAPHNE, Phys. Lett. B **622**, 35 (2005).

[63] T. Miyoshi, M. Sarsour, L. Yuan, X. Zhu, A. Ahmidouch, P. Ambrozewicz, D. Androic, T. Angelescu, R. Asaturyan, S. Avery *et al.* (HNSS Collaboration), High Resolution Spectroscopy of the $^{12}_{\Lambda}$B Hypernucleus Produced by the $(e, e'K^+)$ Reaction, Phys. Rev. Lett. **90**, 232502 (2003).

[64] L. Yuan, M. Sarsour, T. Miyoshi, X. Zhu, A. Ahmidouch, D. Androic, T. Angelescu, R. Asaturyan, S. Avery, O. K. Baker *et al.* (HNSS Collaboration), Hypernuclear spectroscopy using the $(e, e'K^+)$ reaction, Phys. Rev. C **73**, 044607 (2006).

[65] L. Tang, C. Chen, T. Gogami, D. Kawama, Y. Han, L. Yuan, A. Matsumura, Y. Okayasu, T. Seva, V. M. Rodriguez *et al.* (HKS JLab E05-115 and E01-011 Collaborations), Experiments with the high resolution kaon spectrometer at JLab Hall C and the new spectroscopy of $^{12}_{\Lambda}$B hypernuclei, Phys. Rev. C **90**, 034320 (2014).

[66] S. Cohen and D. Kurath, Effective interactions for the 1p shell, Nucl. Phys. A **73**, 1 (1965).

[67] E. H. Auerbach, A. J. Baltz, C. B. Dover, A. Gal, S. H. Kahana, L. Ludeking, and D. J. Millener, Hypernuclear spectroscopy in the p shell, Ann. Phys. (NY) **148**, 381 (1983).

[68] W. Brückner, M. A. Faessler, T. J. Ketel, K. Kilian, J. Niewisch, B. Pietrzy, B. Povh, H. G. Ritter, M. Uhrmacher, P. Birien, H. Catz, A. Chaumeaux, J. M. Durand, B. Mayer, J. Thirion, R. Bertini, and O. Bing, Spin-orbit interaction of Lambda particles in nuclei, Phys. Lett. B **79**, 157 (1978).

[69] H. Tamura, R. S. Hayano, H. Outa, and T. Yamazaki, Study of Λ hypernuclei with stopped K^- reaction, Prog. Theor. Phys. Suppl. **117**, 1 (1994).

[70] P. H. Pile, S. Bart, R. E. Chrien, D. J. Millener, R. J. Sutter, N. Tsoupas, J.-C. Peng, S. Mishra, E. V. Hungerford, T. Kishimoto *et al.*, Study of Hypernuclei by Associated Production, Phys. Rev. Lett. **66**, 2585 (1991).

[71] M. Ukai, S. Ajimura, H. Akikawa, D. E. Alburger, A. Banu, R. E. Chrien, G. B. Franklin, J. Franz, O. Hashimoto, T. Hayakawa *et al.* (E930 ('01) Collaboration), γ-ray spectroscopy of $^{16}_{\Lambda}$O and $^{15}_{\Lambda}$N hypernuclei via the ^{16}O(K^-, π^-) reaction, Phys. Rev. C **77**, 054315 (2008).

[72] M. Leuschner, J. R. Calarco, F. W. Hersman, E. Jans, G. J. Kramer, L. Lapikás, G. van der Steenhoven, P. K. A. de Witt Huberts, H. P. Blok, N. Kalantar-Nayestanaki, and J. Friedrich, Quasielastic proton knockout from ^{16}O, Phys. Rev. C **49**, 955 (1994).

[73] G. van der Steenhoven, H. P. Blok, E. Jans, M. de Jong, L. Lapikás, E. N. M. Quint, and P. K. A. de Witt Huberts, Knockout of $1p$ protons from ^{12}C induced by the $(e, e'p)$ reaction, Nucl. Phys. A **480**, 547 (1988).

[74] T. Motoba, Photoproduction of typical hypernuclei, in *Proceedings of the 12th International Conference on Hypernuclear and Strange Particle Physics (HYP2015)*, edited by H. Tamura, A. Dote, B. F. Gibson, T. Harada, E. Hiyama, A. Hosaka, K. Imai, T. Nagae, S. N. Nakamura, A. Ohnishi, and T. Takahashi (JPS Conf. Proc. 17, 2017), p. 011003.